

# Improved Turbulent Lift Momentum Closure for Multiphase Computational Fluid Dynamics

By  
Brian Casel

B.S., Nuclear Engineering Rensselaer Polytechnic Institute, 2017  
M.Eng., Nuclear Engineering Rensselaer Polytechnic Institute, 2017

SUBMITTED TO THE  
DEPARTMENT OF NUCLEAR SCIENCE AND ENGINEERING  
IN PARTIAL FULFILLMENT OF THE REQUIREMENTS FOR THE DEGREE OF  
MASTER OF SCIENCE IN NUCLEAR SCIENCE AND ENGINEERING

AT THE  
MASSACHUSETTS INSTITUTE OF TECHNOLOGY  
FEBRUARY 2020

©2020 Massachusetts Institute of Technology  
All rights reserved.

Signature of Author: \_\_\_\_\_

Brian Casel  
Department of Nuclear Science and Engineering  
January 17, 2020

Certified by: \_\_\_\_\_

Emilio Baglietto, Ph.D.  
Associate Professor of Nuclear Science and Engineering  
Thesis Supervisor

Certified by: \_\_\_\_\_

Matteo Bucci, Ph.D.  
Norman C. Rasmussen Assistant Professor of Nuclear Science and Engineering  
Thesis Reader

Accepted by: \_\_\_\_\_

Ju Li, Ph.D.  
Battelle Energy Alliance Professor of Nuclear Science and Engineering  
and Professor of Materials Science and Engineering  
Chair, Department Committee on Graduate Students



# Improved Turbulent Lift Momentum Closure for Multiphase Computational Fluid Dynamics

by

Brian Casel

Submitted to the Department of Nuclear Science and Engineering  
on January 17, 2020, in partial fulfillment of the  
requirements for the degree of  
Master of Science in Nuclear Science and Engineering

## Abstract

More efficient boiling heat transfer systems in nuclear reactors can help lower the costs of a large, low carbon energy source. Multiphase computational fluid dynamics (M-CFD) can be utilized in the design of these systems, but requires additional modeling for interphase transfer of mass, momentum, and energy [1]. Within the momentum transfer between phases, the interfacial lift force strongly affects the lateral migration of the gas phase in bubbly flow, which strongly impacts the predictions of pressure drop and heat transfer [2]. Recent work from Sugrue has proposed an improved physical representation of the turbulent lift force utilizing a combination of direct numerical simulation (DNS) data and a numerical optimization of the lift coefficient using experimental data [3]. The resulting Sugrue lift model yielded consistent and improved predictions of lateral redistribution of the gas phase in adiabatic air-water experiments; however, application to developing, bubbly flow has shown there is potential to further improve the accuracy of the formulation [4, 5]. In this work, a systematic optimization to the turbulent lift model is performed to adjust the Sugrue model and a new turbulent lift model is proposed. Both formulations out-perform the original Sugrue model on the Hibiki [6] experiment and the new turbulent lift model marginally improves performance on the TOPFLOW [7] experiments. Additionally, machine learning methods including k-nearest neighbors, principal component analysis, linear regression, random forests, and neural networks, are used to analyze M-CFD data to highlight parameters for future modeling. The linear regression and random forest methods both suggest that superficial liquid and gas velocities ( $J_l$  and  $J_g$ ), and slip ratio ( $S$ ) are the three most important variables for modeling the lift coefficient. Additional data is needed to extract more precise modeling information from the candidate machine learning models in future study.

Thesis Supervisor: Emilio Baglietto, Ph.D.

Title: Associate Professor of Nuclear Science and Engineering



## Acknowledgments

First I want to thank my parents for their support through my time in school. Understandably, it took some convincing for them to let me head up north from Florida. Closely behind them, I want to thank my girlfriend Laurel for always being in my corner. Knowing that I had them behind me made every step of the way easier.

Years of working with the Bubble Bros has made them a part of my family that I will never forget. Outstanding work from group alumni Ben, Nazar, and Rosie laid the foundation for my work. Uncounted hours of technical assistance, cluster support, constant advice, and friendship (along with a little sauce) from Ravi, Zach, Julia, Mike, Eli, Ka-Yen, Etienne, Jinyong, Monica, and Ralph got me through the project itself. Even when things got turbulent, the group was there to lift me back up.

My journey would not have been possible without the amazing NSE support staff. I want to specifically acknowledge Marina and the Communication Lab fellows, Brandy, Heather, Pete, Lisa, Rachel, and Jennifer; I can never thank you all enough for helping with everything from keeping the department running, writing help, navigating fellowship paper work, computer support, and to just being there to talk. Lastly, I want to thank both my thesis reader Professor Matteo Bucci and my advisor Professor Emilio Baglietto. I have learned so much from each of you both inside and outside of the classroom.

Of course, this work would not have been possible without financial support from the Nuclear Engineering University Programs (NEUP) Integrated University Program (IUP) fellowship and the Consortium for Advanced Simulation of Light water reactors (CASL) for both I am extremely grateful.



# Contents

<b>1</b>	<b>Motivation and Introduction</b>	<b>17</b>
<b>2</b>	<b>Interfacial Lift Force</b>	<b>21</b>
2.1	Lift Force . . . . .	21
2.2	Lift Modeling . . . . .	23
2.2.1	Sugrue Model Performance on TOPFLOW . . . . .	26
<b>3</b>	<b>Re-formulation of the Sugrue Model</b>	<b>29</b>
3.1	Expanded Optimization Data . . . . .	29
3.2	Model Fitting Procedure . . . . .	32
3.3	Proposal of a New Wobble Number . . . . .	39
3.3.1	Fitting $W_{new}$ . . . . .	40
<b>4</b>	<b>Validation of the New Model</b>	<b>41</b>
4.1	Developed Flow . . . . .	41
4.2	Developing Flow . . . . .	44
<b>5</b>	<b>Machine Learning For Data Analysis</b>	<b>49</b>
5.1	Machine Learning Background . . . . .	49
5.1.1	k-NN . . . . .	49
5.1.2	Principal Component Analysis . . . . .	50
5.1.3	Linear Regression . . . . .	50
5.1.4	Random Forests . . . . .	51
5.1.5	Neural Networks . . . . .	51

5.2	Leveraging Machine Learning as a Data Analysis Tool . . . . .	52
5.2.1	Data Flow . . . . .	52
5.2.2	Method Settings . . . . .	53
5.2.3	Variable Importance Calculations . . . . .	54
5.3	Insights for Lift Modeling from Machine Learning . . . . .	54
<b>6</b>	<b>Conclusions and Future Work</b>	<b>59</b>
<b>A</b>	<b>Model Implementation in STAR-CCM+</b>	<b>67</b>
<b>B</b>	<b>Hibiki Experiment</b>	<b>71</b>
B.1	Experimental Description . . . . .	71
B.2	Simulation Set Up . . . . .	72
B.3	Velocity Results . . . . .	74
<b>C</b>	<b>TOPFLOW Experiment</b>	<b>81</b>
C.1	Experimental Description . . . . .	81
C.2	Simulation Set Up . . . . .	83
C.3	Velocity Results . . . . .	85
<b>D</b>	<b>Fully Developed Bubbly Flow</b>	<b>91</b>
<b>E</b>	<b>Changes from the Sugrue Model</b>	<b>93</b>



# List of Figures

1-1	Qualitative gas volume fraction predictions (orange lines) using the Tomiyama [8] lift model on the Hibiki experiment [6], from Sugrue [3]	18
1-2	Wall-peaked $\alpha_g$ predictions from Sugrue model (green) on TOPFLOW experiments [7] a) 028 (left) and b) 072 (right) where core-peaked $\alpha_g$ profiles are expected [4]	20
2-1	Schematic representation of how the shape of the $\alpha_g$ distribution changes as $C_L$ goes from positive (red) to near zero (green) to negative (blue)	22
2-2	Sugrue predictions of $\alpha_g$ on the Hibiki experiment [3]	26
2-3	TOPFLOW cases 028 (left), 050 (center), and 072 (right) simulated with the MIT-Model (which includes the Sugrue lift) where wall-peaks in $\alpha_g$ are predicted when core-peaked $\alpha_g$ distributions are expected [5]	27
3-1	Resulting $\alpha_g$ profiles as $C_L$ changes from -0.1 (blue) to 0.1 (red) for the Hibiki experiment 1_1 (top left), 1_2 (top right), 1_3 (bottom left), and 1_4 (bottom right)	30
3-2	Resulting $\alpha_g$ profiles as $C_L$ changes from -0.1 (blue) to 0.1 (red) for the Hibiki experiment 2_1 (top left), 2_2 (top right), 2_3 (bottom left), and 2_4 (bottom right)	30
3-3	Resulting $\alpha_g$ profiles as $C_L$ changes from -0.1 (blue) to 0.1 (red) for the Hibiki experiment 3_1 (top left), 3_2 (top right), 3_3 (bottom left), and 3_4 (bottom right)	31
3-4	Resulting $\alpha_g$ profiles as $C_L$ changes from -0.1 (blue) to 0.1 (red) for the Hibiki experiment 4_1 (left) and 4_2 (right)	31

3-5	$C_L$ results from minimizing the MAE on the $\alpha_g$ profiles for the Hibiki experiment 1_1 (top left), 1_2 (top right), 1_3 (bottom left), and 1_4 (bottom right) . . . . .	33
3-6	$C_L$ results from minimizing the MAE on the $\alpha_g$ profiles for the Hibiki experiment 2_1 (top left), 2_2 (top right), 2_3 (bottom left), and 2_4 (bottom right) . . . . .	34
3-7	$C_L$ results from minimizing the MAE on the $\alpha_g$ profiles for the Hibiki experiment 3_1 (top left), 3_2 (top right), 3_3 (bottom left), and 3_4 (bottom right) . . . . .	34
3-8	$C_L$ results from minimizing the MAE on the $\alpha_g$ profiles for the Hibiki experiment 4_1 (left) and 4_2 (right) . . . . .	35
3-9	$\alpha_g$ profiles from the optimized $C_L$ values for the Hibiki experiment 1_1 (top left), 1_2 (top right), 1_3 (bottom left), and 1_4 (bottom right)	35
3-10	$\alpha_g$ profiles from the optimized $C_L$ values for the Hibiki experiment 2_1 (top left), 2_2 (top right), 2_3 (bottom left), and 2_4 (bottom right)	36
3-11	$\alpha_g$ profiles from the optimized $C_L$ values for the Hibiki experiment _1 (top left), 3_2 (top right), 3_3 (bottom left), and 3_4 (bottom right)	36
3-12	$\alpha_g$ profiles from the optimized $C_L$ values for the Hibiki experiment 4_1 (left) and 4_2 (right) . . . . .	37
3-13	Resulting adjusted fitting values of $C_L$ from minimization of MAE in $\alpha_g$ on the Hibiki experiment . . . . .	37
3-14	Newly proposed model compared to the Sugrue model . . . . .	38
3-15	$Wo_{new}$ model from fitting with Hibiki optimization . . . . .	40
4-1	Comparison of $\alpha_g$ profiles from Sugrue, the adjusted Sugrue, and $Wo_{new}$ on Hibiki 1_1 (top left), 1_2 (top right), 1_3 (bottom left), and 1_4 (bottom right) . . . . .	42
4-2	Comparison of $\alpha_g$ profiles from Sugrue, the adjusted Sugrue, and $Wo_{new}$ on Hibiki 2_1 (top left), 2_2 (top right), 2_3 (bottom left), and 2_4 (bottom right) . . . . .	42

4-3	Comparison of $\alpha_g$ profiles from Sugrue, the adjusted Sugrue, and $Wo_{new}$ on Hibiki 3_1 (top left), 3_2 (top right), 3_3 (bottom left), and 3_4 (bottom right) . . . . .	43
4-4	Comparison of $\alpha_g$ profiles from Sugrue, the adjusted Sugrue, and $Wo_{new}$ on Hibiki 4_1 (left) and 4_2 (right) . . . . .	43
4-5	Spread error on $\alpha_g$ profiles from Sugrue, the adjusted Sugrue, and $Wo_{new}$ on Hibiki experiment . . . . .	44
4-6	Comparison of $\alpha_g$ profiles from Sugrue, the adjusted Sugrue, and $Wo_{new}$ on TOPFLOW 006 (left) and 008 (right) . . . . .	45
4-7	Comparison of $\alpha_g$ profiles from Sugrue, the adjusted Sugrue, and $Wo_{new}$ on TOPFLOW 028 (left) and 030 (right) . . . . .	46
4-8	Comparison of $\alpha_g$ profiles from Sugrue, the adjusted Sugrue, and $Wo_{new}$ on TOPFLOW 050 (left) and 052 (right) . . . . .	46
4-9	Comparison of $\alpha_g$ profiles from Sugrue, the adjusted Sugrue, and $Wo_{new}$ on TOPFLOW 072 (left) and 074 (right) . . . . .	47
4-10	Spread error on $\alpha_g$ profiles from Sugrue, the adjusted Sugrue, and $Wo_{new}$ on TOPFLOW experiment . . . . .	48
5-1	Comparison of $C_L$ predictions from machine learning methods to the human analysis . . . . .	55
5-2	Training and validation errors for the neural network . . . . .	57
5-3	Comparison of variable importances from linear regression, random forest, and PCA . . . . .	58
B-1	Hibiki computational mesh . . . . .	73
B-2	Comparison of $U_l$ profiles from Sugrue, the adjusted Sugrue, and $Wo_{new}$ on Hibiki 1_1 (top left), 1_2 (top right), 1_3 (bottom left), and 1_4 (bottom right) . . . . .	74
B-3	Comparison of $U_l$ profiles from Sugrue, the adjusted Sugrue, and $Wo_{new}$ on Hibiki 2_1 (top left), 2_2 (top right), 2_3 (bottom left), and 2_4 (bottom right) . . . . .	75

B-4	Comparison of $U_l$ profiles from Sugrue, the adjusted Sugrue, and $Wo_{new}$ on Hibiki 3_1 (top left), 3_2 (top right), 3_3 (bottom left), and 3_4 (bottom right) . . . . .	75
B-5	Comparison of $U_l$ profiles from Sugrue, the adjusted Sugrue, and $Wo_{new}$ on Hibiki 4_1 (left) and 4_2 (right) . . . . .	76
B-6	Comparison of $U_g$ profiles from Sugrue, the adjusted Sugrue, and $Wo_{new}$ on Hibiki 1_1 (top left), 1_2 (top right), 1_3 (bottom left), and 1_4 (bottom right) . . . . .	76
B-7	Comparison of $U_g$ profiles from Sugrue, the adjusted Sugrue, and $Wo_{new}$ on Hibiki 2_1 (top left), 2_2 (top right), 2_3 (bottom left), and 2_4 (bottom right) . . . . .	77
B-8	Comparison of $U_g$ profiles from Sugrue, the adjusted Sugrue, and $Wo_{new}$ on Hibiki 3_1 (top left), 3_2 (top right), 3_3 (bottom left), and 3_4 (bottom right) . . . . .	77
B-9	Comparison of $U_g$ profiles from Sugrue, the adjusted Sugrue, and $Wo_{new}$ on Hibiki 4_1 (left) and 4_2 (right) . . . . .	78
B-10	Spread error on $U_l$ profiles from Sugrue, the adjusted Sugrue, and $Wo_{new}$ on Hibiki experiment . . . . .	78
B-11	Spread error on $U_g$ profiles from Sugrue, the adjusted Sugrue, and $Wo_{new}$ on Hibiki experiment . . . . .	79
C-1	TOPFLOW test section and air injectors of study [7] . . . . .	82
C-2	TOPFLOW computational mesh . . . . .	84
C-3	Comparison of $U_l$ profiles from Sugrue, the adjusted Sugrue, and $Wo_{new}$ on TOPFLOW 006 (left) and 008 (right) . . . . .	85
C-4	Comparison of $U_l$ profiles from Sugrue, the adjusted Sugrue, and $Wo_{new}$ on TOPFLOW 028 (left) and 030 (right) . . . . .	86
C-5	Comparison of $U_l$ profiles from Sugrue, the adjusted Sugrue, and $Wo_{new}$ on TOPFLOW 050 (left) and 052 (right) . . . . .	86

C-6	Comparison of $U_l$ profiles from Sugrue, the adjusted Sugrue, and $Wo_{new}$ on TOPFLOW 072 (left) and 074 (right) . . . . .	87
C-7	Comparison of $U_g$ profiles from Sugrue, the adjusted Sugrue, and $Wo_{new}$ on TOPFLOW 006 (left) and 008 (right) . . . . .	87
C-8	Comparison of $U_g$ profiles from Sugrue, the adjusted Sugrue, and $Wo_{new}$ on TOPFLOW 028 (left) and 030 (right) . . . . .	88
C-9	Comparison of $U_g$ profiles from Sugrue, the adjusted Sugrue, and $Wo_{new}$ on TOPFLOW 050 (left) and 052 . . . . .	88
C-10	Comparison of $U_g$ profiles from Sugrue, the adjusted Sugrue, and $Wo_{new}$ on TOPFLOW 072 (left) and 074 (right) . . . . .	89
C-11	Spread error on $U_g$ profiles from Sugrue, the adjusted Sugrue, and $Wo_{new}$ on TOPFLOW experiment . . . . .	89
D-1	Comparison of the developing $\alpha_g$ profile from TOPFLOW 074 (left) to Hibiki 3_2 (right), showing that Hibiki experiments 3_1 and 3_2 may not be fully developed flow . . . . .	92
E-1	Sugrue difference and difficulty on Hibiki 2_4 . . . . .	93
E-2	Sugrue difference and difficulty on Hibiki 4_1 . . . . .	94
E-3	Sugrue difference and difficulty on Hibiki 4_2 . . . . .	94



# List of Tables

5.1	Tabulated $C_L$ values from k-NN, linear regression (LR), random forest (RF), and neural networks (NN) machine learning methods . . . . .	55
B.1	Summary of Hibiki conditions [6] . . . . .	72
C.1	TOPFLOW air injector distance from sensor [7] . . . . .	82
C.2	Summary of TOPFLOW conditions [7] . . . . .	83





# Chapter 1

## Motivation and Introduction

High capital cost is one of the biggest challenges facing nuclear power today. While new system designs and components have the potential to improve safety and reduce these costs, their adoption requires extensive testing. Building and testing nuclear reactor components can be very expensive and take a long time, prohibiting design updates. To reduce total costs and produce optimal designs in a shorter time span, high fidelity simulations can be applied to replace early design and testing phases.

Multiphase computational fluid dynamics (M-CFD) can be leveraged to simulate flows typically observed in boiling heat transfer systems, such as boiling water reactor (BWR) and pressurized water reactor (PWR) sub-channels and PWR steam generators. High fidelity simulations of these systems could be used as a powerful 3D design tool in place of geometry dependent correlations. Currently, M-CFD cannot accurately model all of the flow regimes that occur in these systems. The first regime to occur after the onset of boiling is bubbly flow, which is the area of focus in this work. Bubbly flow can be modeled using the most general approach to model multiphase flows, the two fluid, Eulerian-Eulerian averaging approach. The averaging process introduces additional interfacial mass, momentum and energy terms which require modeling.

Adiabatic experiments are the simplest multiphase systems to model. These exper-

iments isolate the interfacial momentum transfer since there is no interphase mass (e.g., boiling) or energy transfer (e.g., heat convection) [1]. Replicating these experiments allows for the derivation of more physically consistent models for interfacial momentum transfer, due to the elimination of errors coming from incorrect modeling of interphase mass and energy transfer. The momentum transfer described by the interfacial lift force drives the migration of the gas phase perpendicular to the flow direction. This lateral migration is due to inertial effects in viscous flow that are driven by the velocity gradient in the liquid flow. Changes in the lateral distribution of the gas phase as a result of the lift force greatly affect the hydrodynamics of the flow [2]. Therefore it is essential to model lift correctly as a first step towards being able to use M-CFD for the design of boiling heat transfer systems in nuclear reactors.

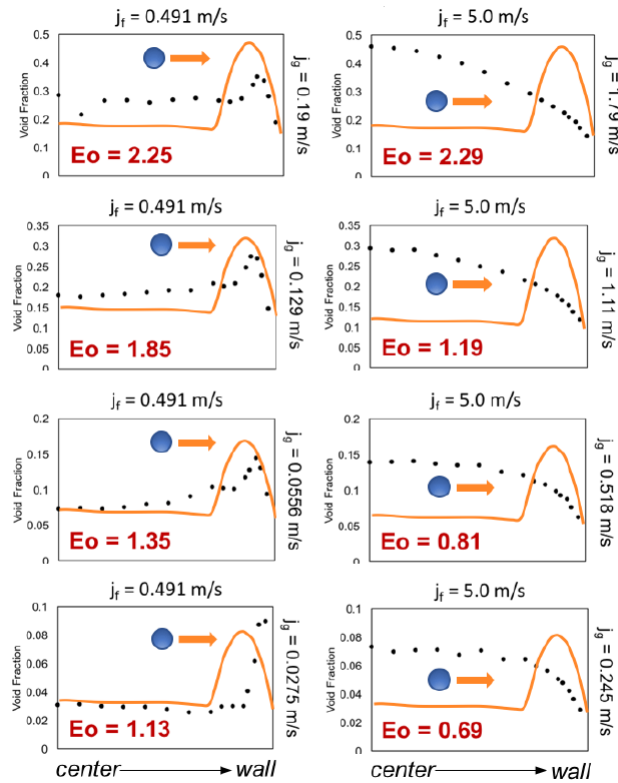


**Figure 1-1:** Qualitative gas volume fraction predictions (orange lines) using the Tomiyama [8] lift model on the Hibiki experiment [6], from Sugrue [3]

Sugrue well identified the shortcomings of extending the existing, laminar lift closure from Tomiyama [8]. Utilizing Eötvös number ( $Eo$ ), a measure of bubble deformability

from fluid and bubble properties, the Tomiyama model always predicts a wall-peaked gas volume fraction ( $\alpha_g$ ) distribution for the Hibiki experiment [6], depicted in Figure 1-1 [3]. However, within the Hibiki experimental data there are cases with  $Eo \approx 1-2$  that have both wall-peaked and core-peaked  $\alpha_g$  profiles [3]. Using solely  $Eo$ , both the wall-peaked and core-peaked  $\alpha_g$  profiles seen in Hibiki can not be predicted. The  $Eo$  number alone is not sufficient to describe the lateral migration of bubbles in turbulent flow conditions [3].

The assertion that  $Eo$  alone cannot capture the lift force was echoed by recent work from Kommajosyula [9]. When developing a 1D correlation for use in sub-channel codes, Kommajosyula also found that only  $Eo$  was not enough to capture the lift inversion from studying the average flow data from multiple bubbly flow experiments. Instead, it was postulated to use a combination of both  $Eo$  and liquid Reynolds number ( $Re_l$ ), a measure of turbulence, to determine if a flow was wall or core-peaked. Additionally, experimental study of the effects of turbulence on bubbles is being performed at John Hopkins. In their experiments, bubbles are released into a downwards flow with jets controlling the turbulence levels to study bubble deformation and break up [10].

The limits of the Sugrue model were shown by Shiea [4] in the analysis of developing, bubbly flows from the TOPFLOW experiment [8]. In two cases of the TOPFLOW experiment where core-peaked  $\alpha_g$  distributions were observed experimentally, wall-peaked profiles were predicted by the Sugrue model, shown in Figure 1-2 [4]. There is potential to further improve the accuracy and generality of the Sugrue model to better capture the effects of turbulence on the lift force.

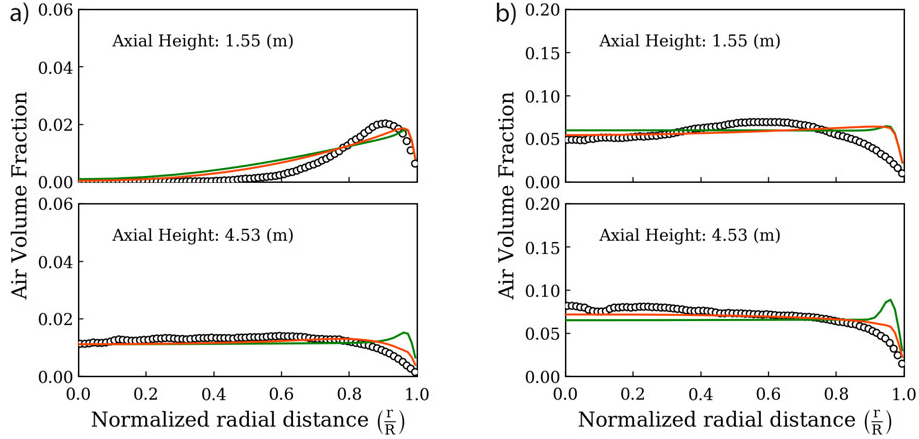


**Figure 1-2:** Wall-peaked  $\alpha_g$  predictions from Sugrue model (green) on TOPFLOW experiments [7] a) 028 (left) and b) 072 (right) where core-peaked  $\alpha_g$  profiles are expected [4]

The objectives for this thesis are:

1. Expand the accuracy and generality of the Sugrue model using data from the fully developed, two-phase flow experiment from Hibiki and the developing, two-phase flow experiment TOPFLOW.
2. Leverage advanced machine learning and data processing tools to study M-CFD data and gain physical insights for future model advancements.

Topics related to Objective 1 are discussed in Chapters 2-4. In Chapter 2 there is a discussion of the lift force and previous modeling efforts. In Chapter 3 a re-formulation of the Sugrue lift model is performed and a new  $Wo$  is proposed. In Chapter 4 the newly proposed models are validated on the Hibiki and TOPFLOW experiments. In Chapter 5 background information on the machine learning tools used is provided. Additionally, Chapter 5 presents predictions of  $C_L$  made from the experimental data after training machine learning models on M-CFD data along with a study of variable importance for modeling  $C_L$ . Lastly, Chapter 6 provides the conclusions and areas for future work.

# Chapter 2

## Interfacial Lift Force

### 2.1 Lift Force

In two-phase flow where water is the continuous phase and air is the dispersed phase, using the Eulerian-Eulerian framework, the interfacial lift force is modeled as

$$F_L = -C_L \alpha_g \rho_l |U_r| \times (\nabla \times U_l) \quad (2.1)$$

where  $C_L$  is the lift coefficient,  $\rho_l$  is the liquid density, and  $U_r$  is the relative velocity between the gas and liquid phases ( $U_g - U_l$ ) [1]. A considerable amount of effort has gone into modeling  $C_L$ : analytic derivations modeling spheres in shear flows, single bubble experiments, and both direct numerical simulation (DNS) and M-CFD simulations of single and multi-bubble systems [3, 8, 11, 12, 13, 14, 15, 16]. The lateral migration of the gas phase and the resulting  $\alpha_g$  distribution for bubbly flow is dominantly driven by the lift force.

In fully developed, upward, bubbly, pipe flow the sign of  $C_L$  either drives the gas phase towards the wall (if positive) or towards the center of the pipe (if negative) [3]. The transition of the  $\alpha_g$  profile from wall-peaked to core-peaked is shown schematically by the red and blue lines in Figure 2-1 below. Both of these  $\alpha_g$  distributions can be observed in experimental data [6]. Meanwhile, other momentum closures like wall

lubrication, turbulent dispersion, and drag have smaller effects. Wall lubrication, as defined by Lubchenko, is an artificial force which shapes the  $\alpha_g$  profile within one bubble radius from the wall through a regularization of turbulent dispersion to reflect the geometric constraints of a bubble sliding along the wall [17]. Turbulent dispersion acts to smooth out peaks in the  $\alpha_g$  distribution [18]. In the absence of any lift force, the effects of turbulent dispersion would result in a flat  $\alpha_g$  profile in the bulk of the flow while wall lubrication would cause a drop in  $\alpha_g$  near the wall (shown with the green line in Figure 2-1). Lastly, drag shifts the whole  $\alpha_g$  distribution up or down as drag increases or decreases respectively.

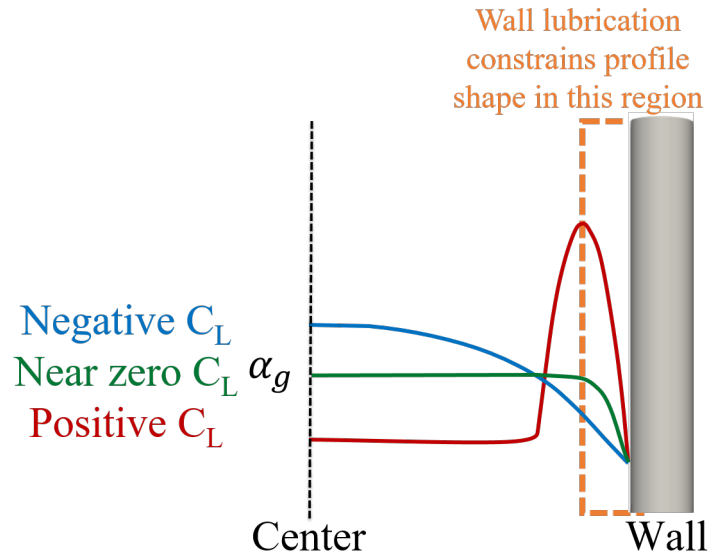


**Figure 2-1:** Schematic representation of how the shape of the  $\alpha_g$  distribution changes as  $C_L$  goes from positive (red) to near zero (green) to negative (blue)

Wall-peaked  $\alpha_g$  distributions lead to flatter liquid velocity ( $U_l$ ) profiles, which reduces wall shear stress ( $\tau_w$ ) and the resulting turbulent kinetic energy ( $k$ ). Meanwhile, core-peaked  $\alpha_g$  distributions result in liquid velocities more similar to those seen in single phase flow [2]. The transition from a positive to a negative  $C_L$  is referred to as "lift inversion." The lift inversion affects pressure drops and the wall heat transfer coefficient, which are critical for design. Since lumped parameter codes are currently used in design of nuclear systems, there even is a desire to capture whether a bubbly flow is wall or core-peaked leveraging average flow parameters [9]. In M-CFD, getting

the correct local  $C_L$  values is crucial to predicting the correct  $\alpha_g$  distribution which is a requirement to accurately model boiling heat transfer systems. In order for M-CFD to be a viable, 3D design tool for nuclear systems  $C_L$  must be accurately resolved locally.

## 2.2 Lift Modeling

The first analytic expression of the lift force was derived by Saffman assuming a slowly rotating sphere moving through a viscous liquid with  $Re_l = 0$  and an infinite shear ratio [11]. The lift force formulated by Saffman was extended to arbitrary shear rates through a proposed  $C_L$  model from McLaughlin using DNS [13]. Another analytic expression of the lift force was derived by Auton assuming a spherical body moving in an inviscid rotational flow with a weak, uniform shear [12]. Legendre and Magnaudet proposed an empirical  $C_L$  correlation for the lift force proposed by Auton using DNS of a spherical bubble in a viscous, linear shear flow [15]. At low  $Re_l$  the correlation for  $C_L$  from Legendre and Magnaudet reduced back to the solution derived by Saffman and at high  $Re_l$   $C_L$  reduced back to 0.5 as proposed by Auton [15]. From the work by Legendre and Magnaudet it was revealed that at low  $Re_l$ ,  $C_L$  depends strongly on  $Re_l$  and the shear rate, while at moderate to high  $Re_l$  these dependencies were weak [3, 15].

One of the most notable  $C_L$  models that is used today was derived from experiments by Tomiyama. Single bubbles were released in glycerol-water solutions with varying, constant velocity gradients as driven by a belt. Using high speed video, the size and shapes of rising bubbles were measured along with how far they migrated laterally, to calculate the traverse lift force. It was observed that smaller, more spherical bubbles travelled in the direction of the decreasing velocity, corresponding to a positive  $C_L$ . Meanwhile, larger more deformable bubbles travelled the opposite direction, corresponding to a negative  $C_L$  [8]. The resulting Tomiyama lift model captures how the lift force is initially driven by the shear from liquid velocity gradient but then inverts

and comes from the slanted wake behind the bubble [8].

This transition was modeled via the bubble deformability as captured with the bubble Reynolds number,

$$\text{Re}_b = \frac{\rho_l |U_r| d_b}{\mu_l}, \quad (2.2)$$

and Eötvös number,

$$\text{Eo} = \frac{g(\rho_l - \rho_g)d_b^2}{\sigma}, \quad (2.3)$$

where  $d_b$  is the bubble diameter,  $\mu_l$  is the liquid viscosity,  $g$  is the gravitational constant, and  $\sigma$  is the surface tension. The final model is

$$C_L = \begin{cases} \min[0.288 \tanh 0.121 \text{Re}_b, f(\text{Eo}_d)] & \text{Eo}_d < 4 \\ f(\text{Eo}_d) & 4 \leq \text{Eo}_d \leq 10.7 \end{cases} \quad (2.4)$$

where

$$f(\text{Eo}_d) = 0.00105 \text{Eo}_d^3 - 0.0159 \text{Eo}_d^2 - 0.0204 \text{Eo}_d + 0.474 \quad (2.5)$$

and the subscript  $d$  means that for  $\text{Eo}$  the maximum horizontal width of the bubble is used as the bubble diameter [8]. The lift inversion occurs at  $\text{Eo}_d \approx 6.062$  or  $\text{Eo} \approx 4.592$ .

The Tomiyama lift model was cleverly derived for laminar flows but cannot reproduce the transition from wall-peaked to core-peaked  $\alpha_g$  distributions seen in turbulent bubbly flow experiments [4, 19, 20]. In the absence of an adequate lift model for turbulent conditions, the M-CFD community has tried for a long time to leverage the Tomiyama model in turbulent regimes [21, 22]. It was soon noted that the model predicts  $C_L$  values an order of magnitude higher than what is appropriate for turbulent, bubbly flow conditions [3, 20, 23]. Additionally, in DNS work Liu and Trygvasson found that at  $\text{Re}_l = 3,786$  the lift inversion occurred at  $\text{Eo} = 2.5$  [2]. Therefore Sugrue developed a model for the turbulent lift force utilizing insights from DNS and fully developed,



bubbly flow experiment data [3].

The Sugrue model sought to capture how background turbulence levels cause bubbles to deform and become unstable. Sugrue observed that unstable, "wobbly" bubbles are subject to an inversion of lift and migrate towards the pipe center in upwards, bubbly flow [3]. In order to quantify the tendency of a bubble to destabilize the Wobble number was proposed,

$$\text{Wo} = \text{Eo} \frac{k}{U_r^2}. \quad (2.6)$$

In this formulation  $\text{Eo}$  represents the deformation of the of the bubble without any perturbation from the flow,  $k$  is the turbulent kinetic energy of the liquid which represents the force that destabilizes the bubble, and  $U_r^2$  represents the inertia of the bubble which prevents destabilization. The Sugrue model was developed using the Hibiki experiment which features air and water uniformly injected at the bottom of a pipe and a measurement of the fully developed two-phase flow profile (described in more depth in Appendix B) [3]. The final model from Sugrue was given as

$$C_L = f(\text{Wo})f(\alpha_g) \quad (2.7)$$

where

$$f(\text{Wo}) = \min[0.03, 5.0404 - 5.0781\text{Wo}^{0.0108}] \quad (2.8)$$

captures the lift inversion and

$$f(\alpha_g) = 1.0155 - 1.0154 \exp(8.0506\alpha_g) \quad (2.9)$$

is a correction to reduce lift at high bubble concentrations [3].

The lift inversion occurs in the Sugrue model at  $\text{Wo} = 0.5$ . The resulting  $\alpha_g$  predictions from the Sugrue model on the Hibiki experiment are shown in Figure 2-2. The Sugrue model was validated on three additional fully developed, bubbly flow experiments and reported consistently accurate predictions across a wide array of conditions

[3]. This provided confidence in the concept that the turbulent lift force is different from the force in laminar conditions is accurate.

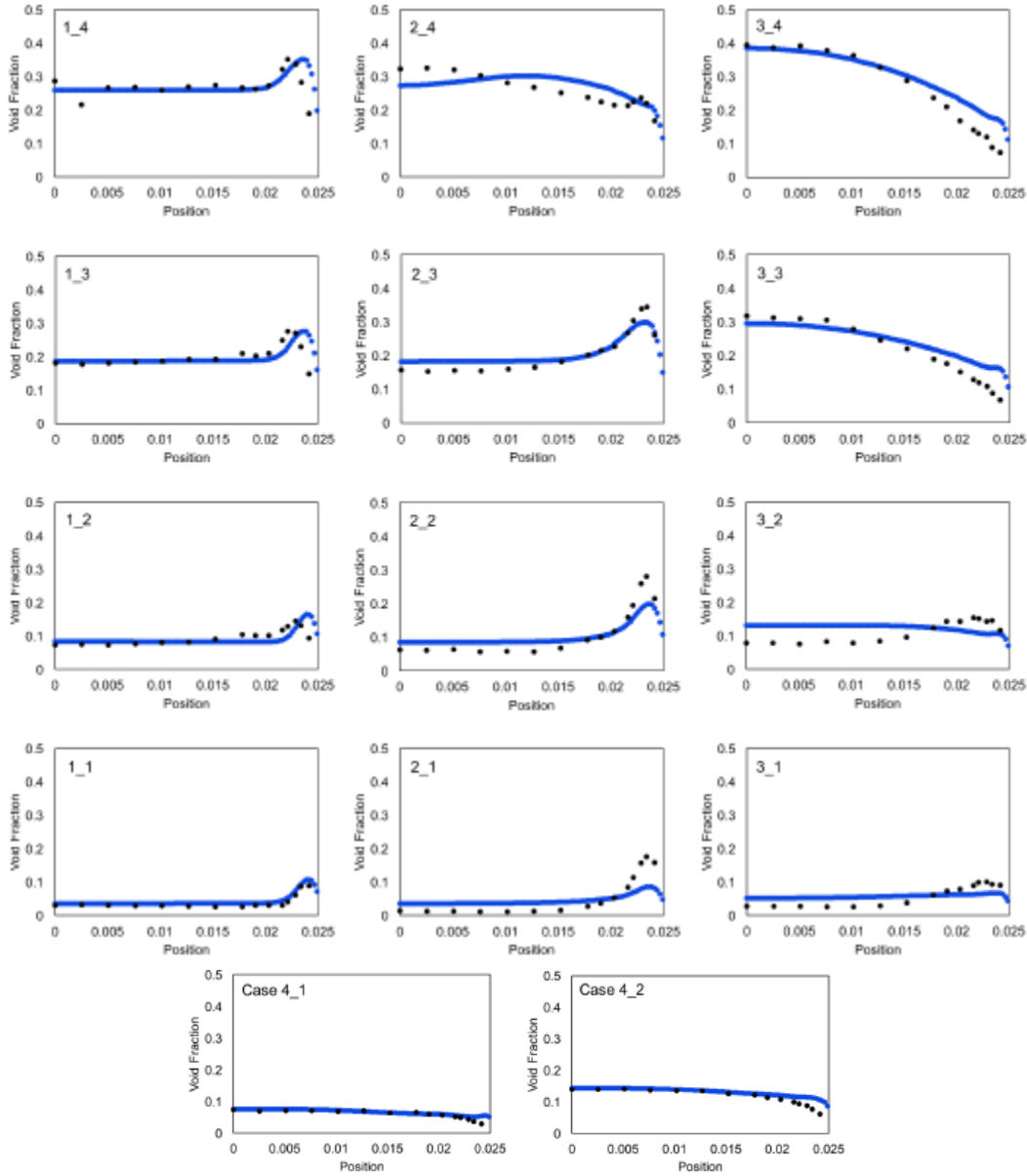
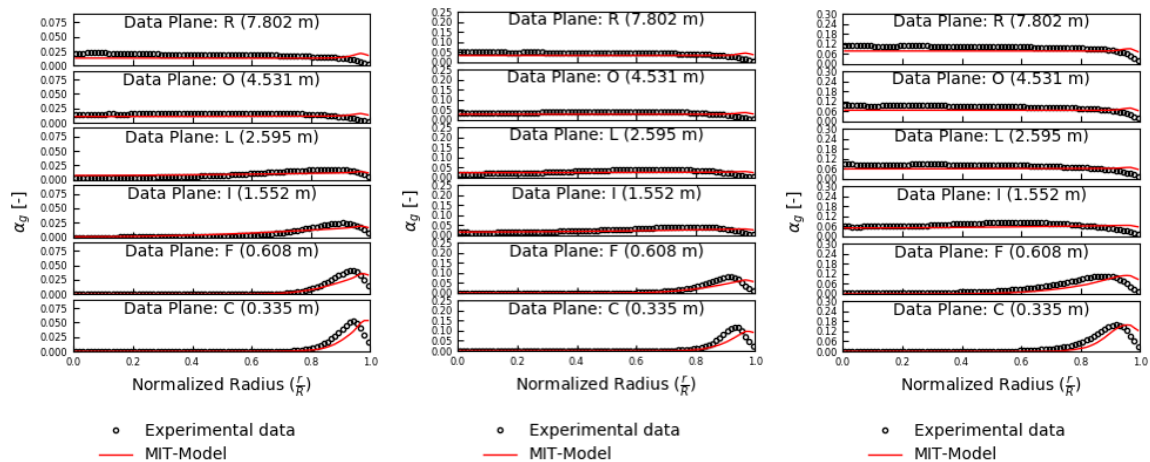


Figure 2-2: Sugrue predictions of  $\alpha_g$  on the Hibiki experiment [3]

### 2.2.1 Sugrue Model Performance on TOPFLOW

The Sugrue model has been further tested on the TOPFLOW experiment [7], which features data taken to recover developing two-phase flow with gas injected at the pipe wall (described in more detail in Appendix C). While the Sugrue model did provide

consistent and stable results on TOPFLOW, the model was unable to correctly predict the exact condition for lift inversion [4] as shown in Figure 1-2. This was also noted by Casel, as shown in Figure 2-3, that for TOPFLOW cases 028, 050, and 072 the MIT-Model (which includes Sugrue lift) predicted wall-peaks in  $\alpha_g$  where core-peaks were expected [5].



**Figure 2-3:** TOPFLOW cases 028 (left), 050 (center), and 072 (right) simulated with the MIT-Model (which includes the Sugrue lift) where wall-peaks in  $\alpha_g$  are predicted when core-peaked  $\alpha_g$  distributions are expected [5]

From an optimization of  $C_L$  using the TOPFLOW experimental  $\alpha_g$  data, Shiea states that the limit on positive  $C_L$  values from the Sugrue model could be too small in magnitude [4]. However, Shiea’s analysis was performed using TOPFLOW data measured 4.5 m downstream from the injection, where the flow may not yet be fully developed (see Appendix D). The Sugrue model demonstrates a strong improvement over the previous models, however continued development in lift modeling is needed. This development was started with a re-formulation of the Sugrue model.



# Chapter 3

## Re-formulation of the Sugrue Model

This chapter details the process performed to advance the formulation of the Sugrue model towards a more accurate prediction of the lift inversion. In order to improve the model performance, the numerical optimization of  $C_L$  on the Hibiki experiment was recreated and expanded to a wider array of  $C_L$  values. With the expanded optimization data, a different statistical analysis was performed in order to refit  $f(\text{Wo})$  (equation 2.8). In addition, a new Wobble number is proposed ( $\text{Wo}_{new}$ ) and fit, attempting to re-characterize the effects of turbulence on lift inversion. The prospective formulations are tested in Chapter 4.

### 3.1 Expanded Optimization Data

Building off the the work from Sugrue [3], 14 cases from the Hibiki experiment [6] were simulated using constant  $C_L$  values. For each case  $C_L$  was varied from -0.1 to 0.1 in 0.001 increments, resulting in 201 simulations. A more in-depth description of the Hibiki experiment and the simulation set-up can be found in Appendix B. Notably, the experimental distribution of sauter mean bubble diameters are used. The results from these simulations are condensed and shown in Figures 3-1 - 3-4. In Figures 3-1 - 3-4, the resulting  $\alpha_g$  distributions from all 201  $C_L$  values are overlaid. As the the value of  $C_L$  goes from -0.1 to 0.1 the color of the curve shifts from blue to red. This data is analyzed in Sections 3.2 and 3.3 for model fitting.

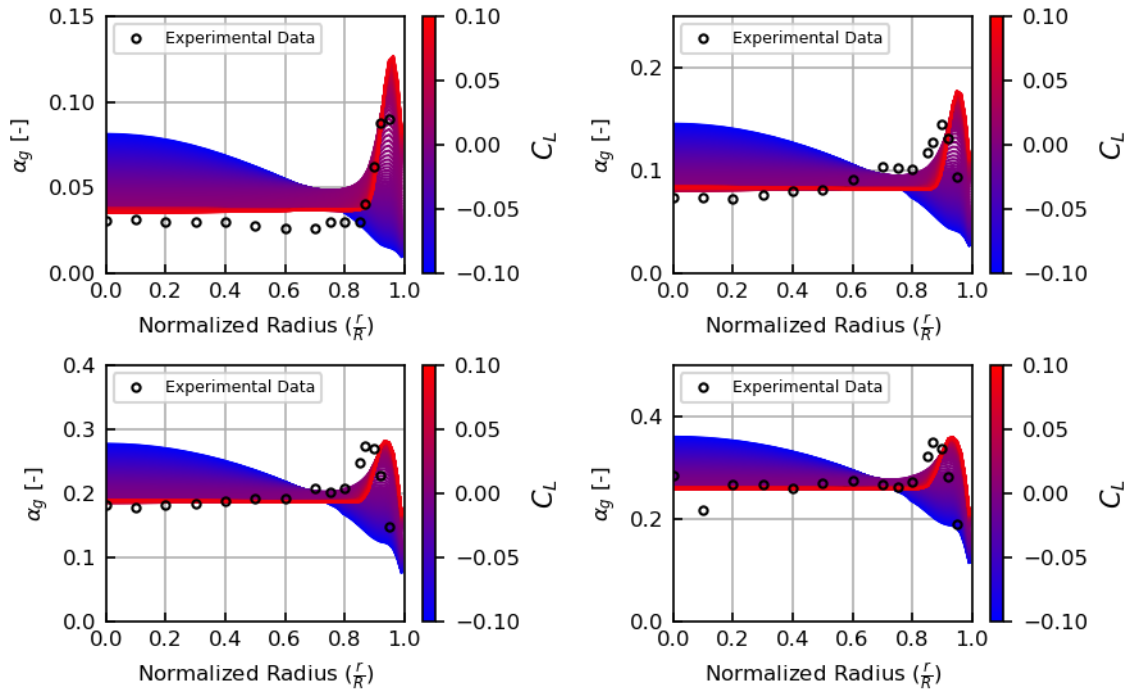


**Figure 3-1:** Resulting  $\alpha_g$  profiles as  $C_L$  changes from -0.1 (blue) to 0.1 (red) for the Hibiki experiment 1\_1 (top left), 1\_2 (top right), 1\_3 (bottom left), and 1\_4 (bottom right)

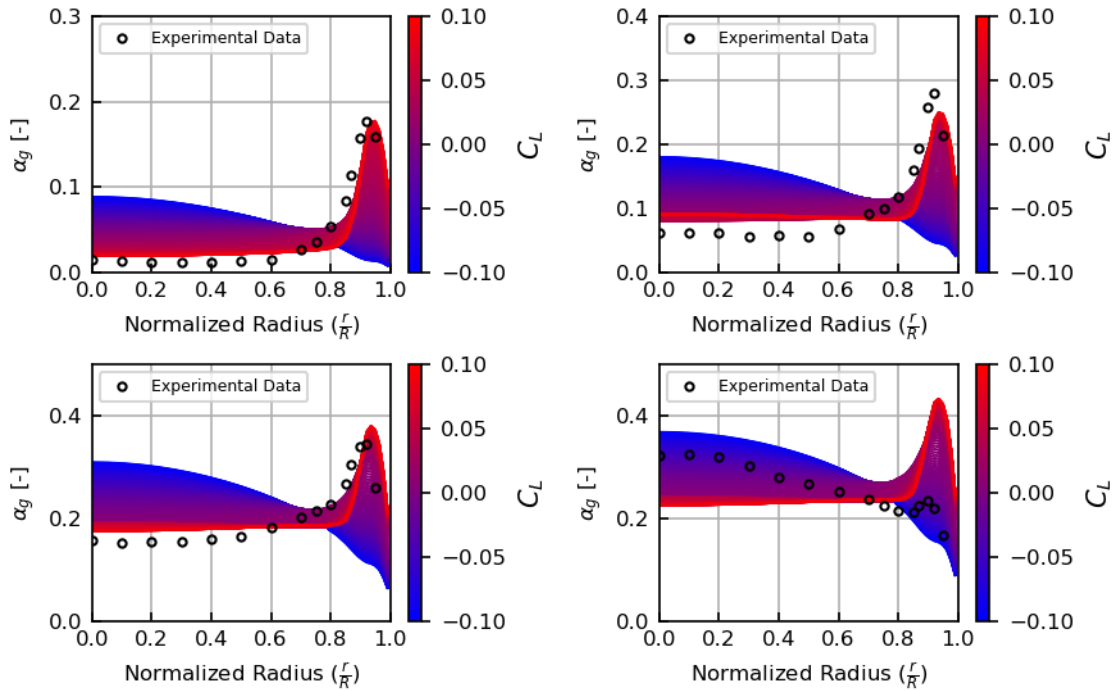


**Figure 3-2:** Resulting  $\alpha_g$  profiles as  $C_L$  changes from -0.1 (blue) to 0.1 (red) for the Hibiki experiment 2\_1 (top left), 2\_2 (top right), 2\_3 (bottom left), and 2\_4 (bottom right)

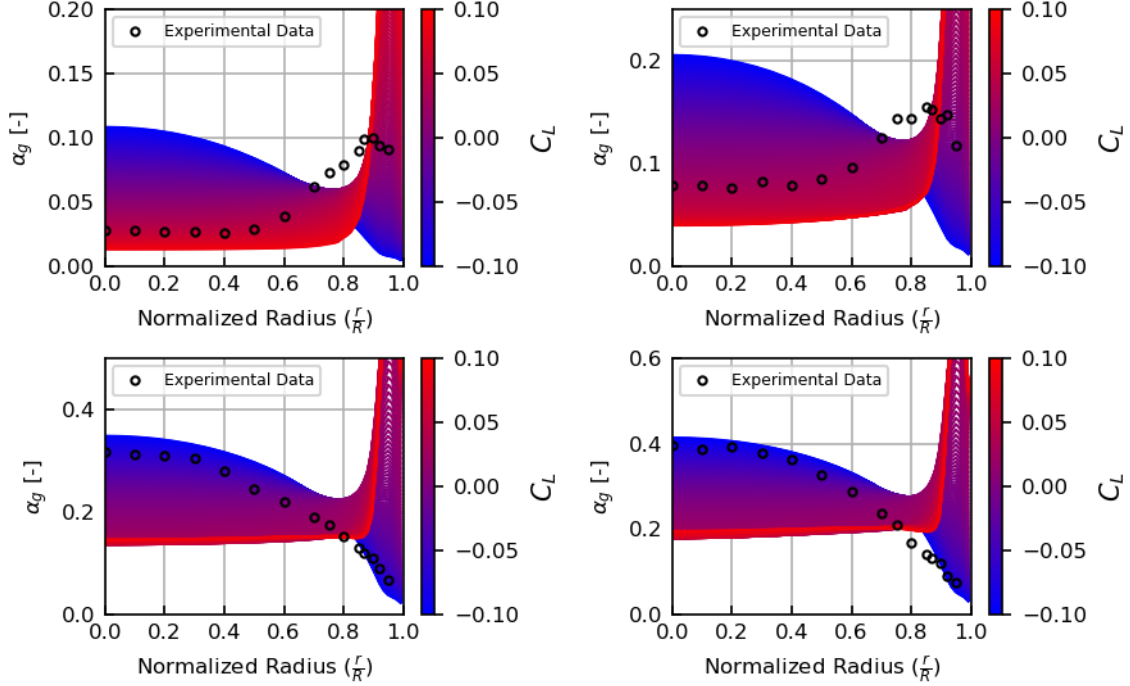


**Figure 3-3:** Resulting  $\alpha_g$  profiles as  $C_L$  changes from -0.1 (blue) to 0.1 (red) for the Hibiki experiment 3\_1 (top left), 3\_2 (top right), 3\_3 (bottom left), and 3\_4 (bottom right)

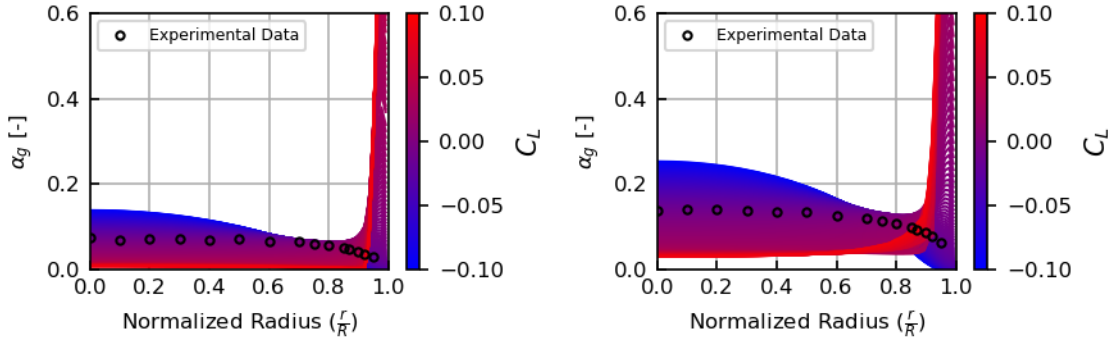


**Figure 3-4:** Resulting  $\alpha_g$  profiles as  $C_L$  changes from -0.1 (blue) to 0.1 (red) for the Hibiki experiment 4\_1 (left) and 4\_2 (right)

It is noticed that while being wall-peaked, the near-wall  $\alpha_g$  peaks for cases 1\_2, 1\_3, 1\_4, 3\_1 and 3\_2 are outside of one bubble radius from the wall. Leveraging the findings from Lubchenko [17], the near-wall  $\alpha_g$  peak should occur within one bubble radius from the wall as it represents the center of the layer of bubble accumulation near the wall. This may point to issues in the experimental data, the selected models, or the assumption that the flow is fully developed. For experiments 1\_2, 1\_3 and

1\_4, it appears that the experimental bubble diameter distribution may be under predicting the bubble size near the wall. With a larger bubble size near the wall, the observed  $\alpha_g$  profile could be captured. For experiments 3\_1 and 3\_2 the  $\alpha_g$  peaks are wide, and are further from one bubble radius than 1\_2, 1\_3, and 1\_4, which could stem from bubbles migrating from the wall back towards the center of the pipe. This may indicate that the flow is not fully developed (discussed further in Appendix D).

Another case of interest is case 2\_4, which appears to be core-peak yet still has a near-wall peak in  $\alpha_g$ . This likely points towards a bi-modal or poly-dispersed bubble size population. Neither a mono-dispersed bubble size or the experimentally measured radial distribution seems able to capture this behavior. Since the focus of this work is to capture the general trend in  $C_L$ , this case will be considered core-peaked; since the dual behavior cannot be captured with the currently selected approach.

## 3.2 Model Fitting Procedure

Utilizing the data presented in Figures 3-1 - 3-4, an adjustment of the Sugrue model was performed. In previous work by Sugrue  $C_L$  was optimized based off the radially averaged absolute different between the experimental and simulation  $\alpha_g$  distributions [3]. One extension in this analysis was to use a different statistical measure for this optimization.

While data-points at a larger radius represent a larger percentage of the pipe area, the radial averaging gives nearly zero weight to points in the pipe center. Meanwhile, at negative  $C_L$  values the void fraction peaks in the pipe center. Therefore, radial weighting could alter the determination of the lift inversion. The optimization in this work was done minimizing the mean absolute error (MAE) between the simulation and the experimental  $\alpha_g$  profiles defined as



$$\text{MAE} = \frac{1}{n} \sum_{i=0}^n |f_{\text{experiment},i} - g_{\text{simulation},i}|. \quad (3.1)$$

Figures 3-5 - 3-8 show the results from the optimization of  $C_L$  using MAE on  $\alpha_g$  for the Hibiki experiment. The resulting  $\alpha_g$  profiles from the optimized  $C_L$  values are shown in Figures 3-9 - 3-12. This ensures that the optimized values capture the general trends from the Hibiki experiment before fitting is performed.

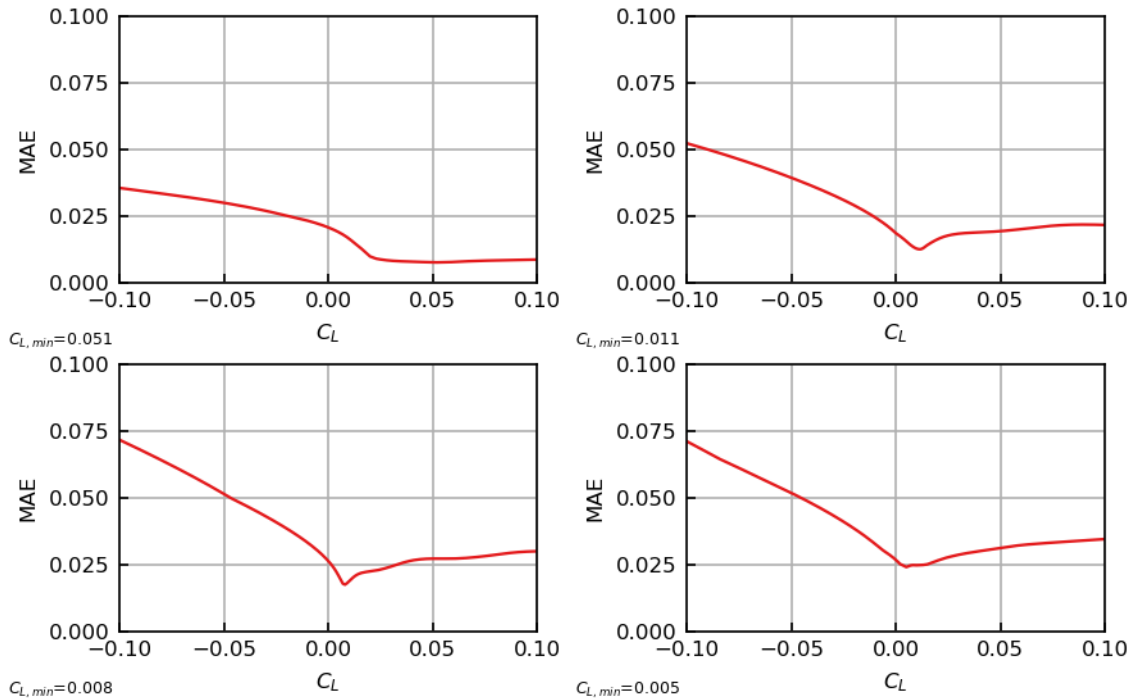


**Figure 3-5:**  $C_L$  results from minimizing the MAE on the  $\alpha_g$  profiles for the Hibiki experiment 1\_1 (top left), 1\_2 (top right), 1\_3 (bottom left), and 1\_4 (bottom right)

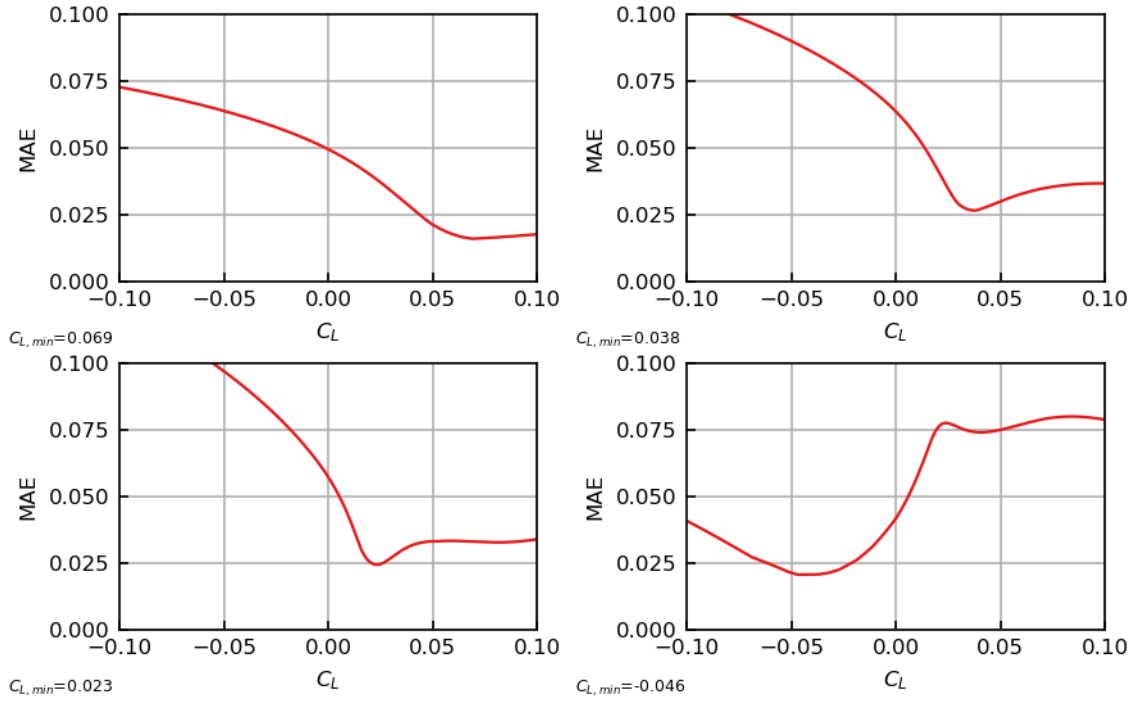


**Figure 3-6:**  $C_L$  results from minimizing the MAE on the  $\alpha_g$  profiles for the Hibiki experiment 2\_1 (top left), 2\_2 (top right), 2\_3 (bottom left), and 2\_4 (bottom right)

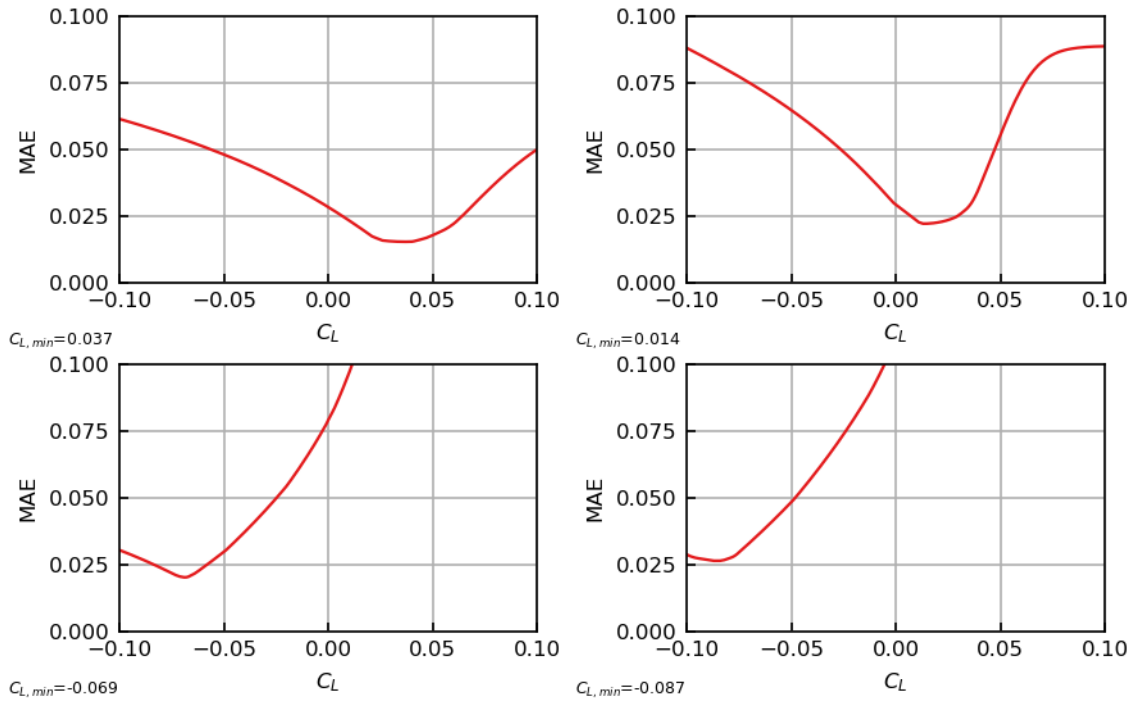


**Figure 3-7:**  $C_L$  results from minimizing the MAE on the  $\alpha_g$  profiles for the Hibiki experiment 3\_1 (top left), 3\_2 (top right), 3\_3 (bottom left), and 3\_4 (bottom right)

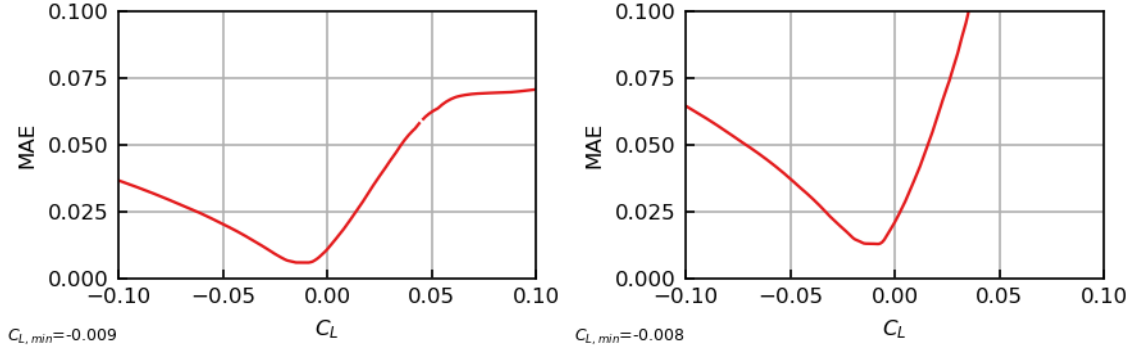


**Figure 3-8:**  $C_L$  results from minimizing the MAE on the  $\alpha_g$  profiles for the Hibiki experiment 4\_1 (left) and 4\_2 (right)

Figures 3-9 - 3-12 show that the optimized  $C_L$  values are reasonable for fitting. However these results, again, show some limitations for the selected models. The constant  $C_L$  values cannot completely capture the  $\alpha_g$  distributions. For example, in several of the wall-peaked cases (1\_1, 1\_2, 2\_1, 2\_2, and 2\_3)  $\alpha_g$  in the center is over-predicted. Meanwhile, in the strongly core-peaked cases (3\_3 and 3\_4) from  $0.4 < \frac{r}{R} < 0.8$ ,  $\alpha_g$  is also over-predicted. Therefore it is necessary to create a general  $C_L$  model to account for the local variation in the coefficient.

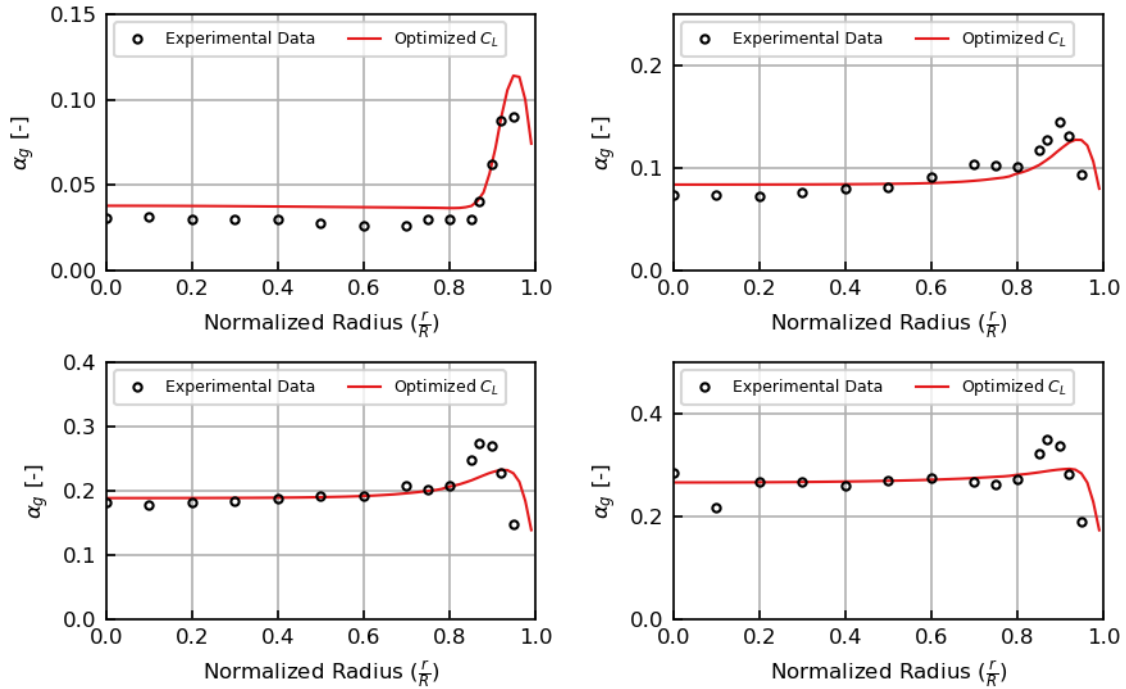


**Figure 3-9:**  $\alpha_g$  profiles from the optimized  $C_L$  values for the Hibiki experiment 1\_1 (top left), 1\_2 (top right), 1\_3 (bottom left), and 1\_4 (bottom right)

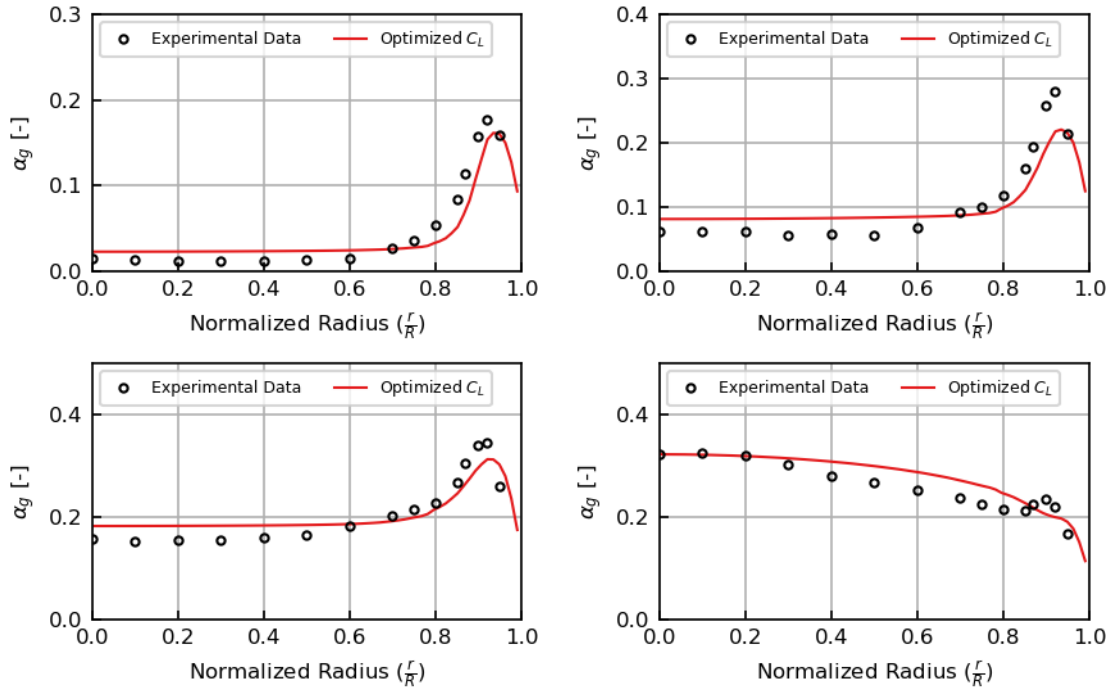


**Figure 3-10:**  $\alpha_g$  profiles from the optimized  $C_L$  values for the Hibiki experiment 2\_1 (top left), 2\_2 (top right), 2\_3 (bottom left), and 2\_4 (bottom right)

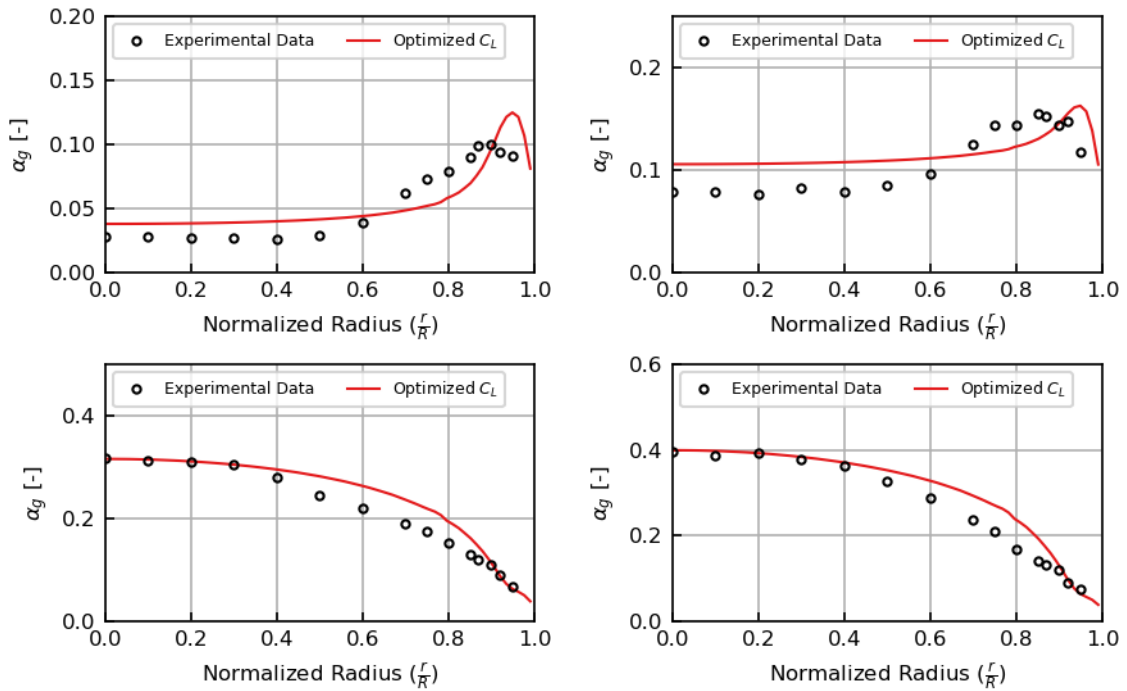


**Figure 3-11:**  $\alpha_g$  profiles from the optimized  $C_L$  values for the Hibiki experiment 3\_1 (top left), 3\_2 (top right), 3\_3 (bottom left), and 3\_4 (bottom right)

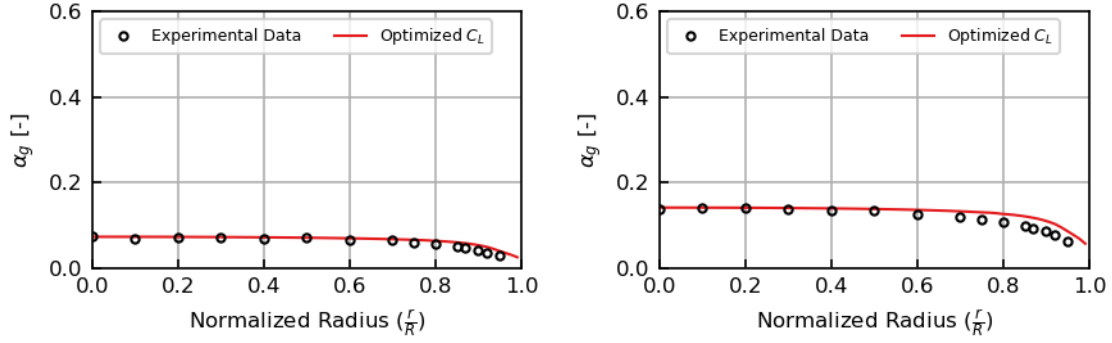


**Figure 3-12:**  $\alpha_g$  profiles from the optimized  $C_L$  values for the Hibiki experiment 4\_1 (left) and 4\_2 (right)

The resulting points for fitting  $C_L$  from the optimization on the Hibiki experiment are shown in Figure 3-13. Figure 3-13 plots the adjusted  $C_L$  values against the radially averaged value of  $Wo$  for each case. The adjusted  $C_L$  value is calculated by dividing the optimized  $C_L$  values from Figures 3-5 - 3-8 by the radially averaged value of  $f(\alpha_g)$  for each case. This provided the needed value of  $f(Wo)$  to get the optimized  $C_L$  value. The error bars in Figure 3-13 represent an error within 10% of the minimum values from Figures 3-5 - 3-8. From these points, the fitting from the Sugrue model was adjusted. Fitting was performed using the same definition for  $Wo$  (equation 2.6) and form of  $f(Wo)$  (equation 2.8) as Sugrue used [3].

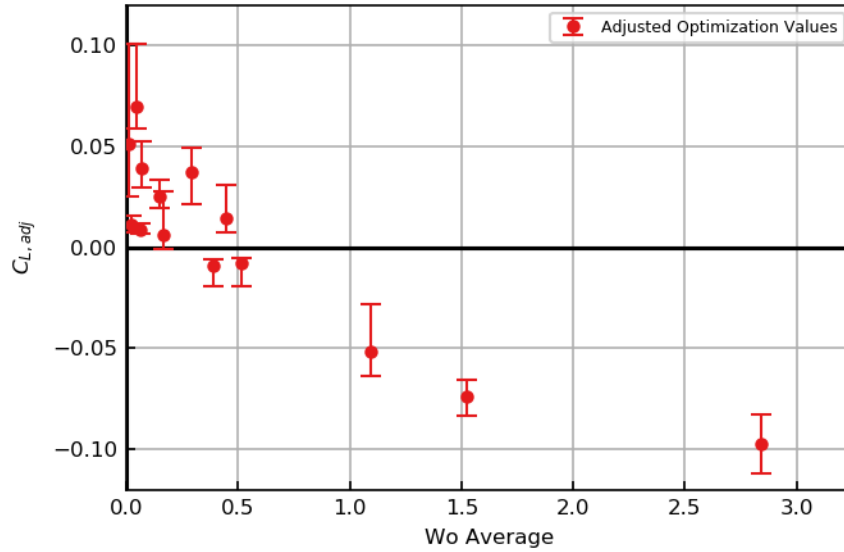


**Figure 3-13:** Resulting adjusted fitting values of  $C_L$  from minimization of MAE in  $\alpha_g$  on the Hibiki experiment

Since previous work had found that a  $C_L$  value  $\approx 0.03$  is optimal for wall-peaked, fully developed, turbulent bubbly flows [20, 23] the max term from equation 2.6 was retained. While it was suggested that 0.03 is too low of a value to capture the TOPFLOW results [4] that conclusion appears to have been made analyzing a non-fully developed flow profile (see Appendix D). Therefore, only the negative  $C_L$  values were used to fit the coefficients for the adjusted Sugrue model. The newly proposed model is shown in Figure 3-14 and compared to the Sugrue model.

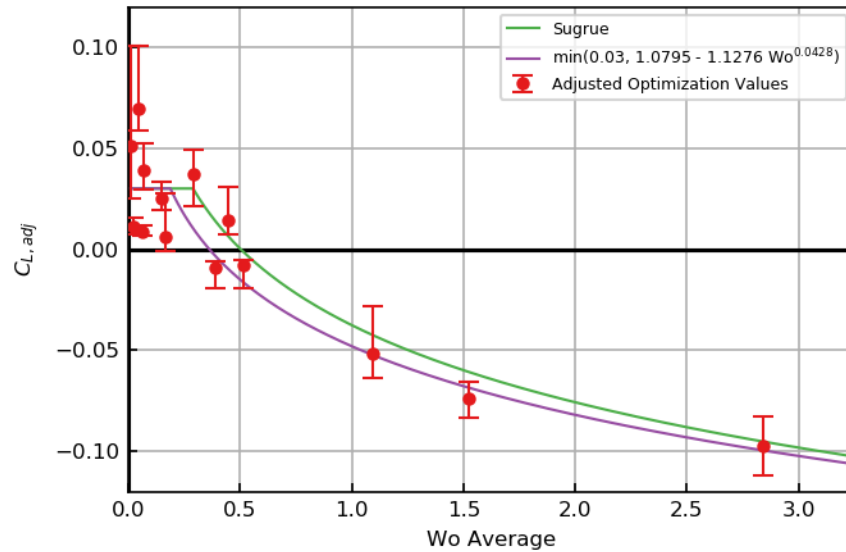


**Figure 3-14:** Newly proposed model compared to the Sugrue model

The newly proposed relation is

$$f(\text{Wo}) = \min(0.03, 1.0795 - 1.1276\text{Wo}^{0.0428}). \quad (3.2)$$

The resulting curve in Figure 3-14 shows a similar shape to the Sugrue model with an earlier lift inversion at  $\text{Wo} \approx 0.36$ . This earlier inversion and adjusted slope is expected to lead to improved performance on the Hibiki experiment (especially on the cases discussed in Appendix E, where the results from Sugrue [3] were not able to be replicated). The performance of the adjusted Sugrue model and the original Sugrue model are compared on the Hibiki and TOPFLOW experiments in Chapter 4.

### 3.3 Proposal of a New Wobble Number

In the original Sugrue model [3],  $Eo$  is directly modified by a turbulence term ( $\frac{k}{U_r^2}$ ) where  $k$  represents the force that destabilizes the bubble and  $U_r^2$  which represents the inertia of the bubble preventing destabilization (equation 2.6). As formulated, the lift inversion occurs at  $Wo = 0.5$ . This definition of  $Wo$  is only applicable to turbulent conditions and reduces to  $Wo = 0$  for laminar conditions. Therefore, for bubbles rising in static fluid,  $Wo$  would always be nearly 0 and a negative  $C_L$  would never be predicted. A goal for this work is to propose a new  $Wo$  ( $Wo_{new}$ ) that is more carefully formulated and could be generally applied for laminar and turbulent conditions. Fitting for  $Wo_{new}$  was performed along side the adjustment of the terms for the original  $Wo$  from Sugrue.

After experimenting with several potential formulations utilizing the data from the Hibiki optimization, a new  $Wo$  is proposed as

$$Wo_{new} = Eo(1 + \frac{\sqrt{k}U_l}{U_r^2})^{1.5}. \quad (3.3)$$

This relationship is inspired by the proposed adjustment in lift modeling to account for bubble induced turbulence (BIT),  $Wo_{BIT}$ , from Magolan [24],

$$Wo_{BIT} = Eo^{0.5}(\frac{\sqrt{k}U_l}{U_r^2})^{1.5}, \quad (3.4)$$

with minor adjustments. The biggest adjustments are that  $Eo$  is not modified to any power and the turbulence term is added to the value one before being multiplied by  $Eo$ . This allows for  $Wo_{new}$  to revert back to  $Eo$  when there no is fluid flow or turbulence and to be more stable when using a BIT model. In this work, a model spanning these two regions is not proposed and instead focus remains on modeling for the turbulent regime. However this formulation allows  $Wo_{new}$  to be used for modeling  $C_L$  across laminar and turbulent conditions in future work.

### 3.3.1 Fitting $Wo_{new}$

Following a similar procedure as used in Section 3.2,  $Wo_{new}$  was fit on the Hibiki optimization data. The only adjustment to the fitting procedure was that the lift inversion point was directly set by adjusting the y-intercept in equation 3.5 based off preliminary testing on the Hibiki database. In the new model, lift inversion occurs at  $Wo_{new} \approx 13$ . The results from this fitting are shown in Figure 3-15.  $Wo_{new}$  does appear to better separate the positive and negative  $C_L$  cases but still does not provide much clarity for the positive  $C_L$  cases. The turbulence term in this formulation will likely need adjustment in future work, but the more general formulation should lead to an improvement over past models.

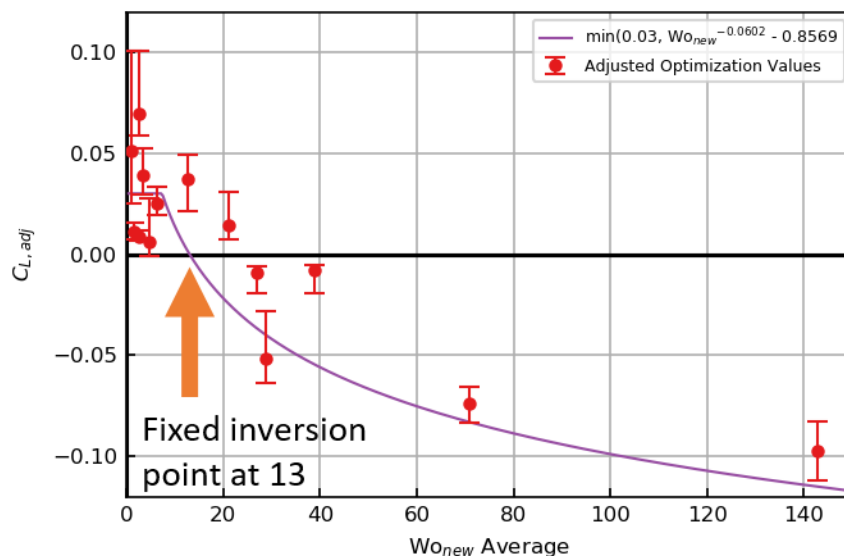


Figure 3-15:  $Wo_{new}$  model from fitting with Hibiki optimization

The relation for  $Wo_{new}$  is

$$f(Wo_{new}) = \min(0.03, Wo_{new}^{-0.0602} - 0.8569). \quad (3.5)$$

This newly proposed model will be tested along with the adjusted Sugrue model on the Hibiki and TOPFLOW experiments in Chapter 4.



# Chapter 4

## Validation of the New Model

### 4.1 Developed Flow

To first test the newly proposed models, they are applied to the simulation of the Hibiki experiment. The Hibiki experiment has a uniform air-water injection and measurements at the end of the pipe where the flow is assumed to be fully developed (for most cases, see Appendix D). A more detailed description of the experiment and the simulation set up can be found in Appendix B. The resulting  $\alpha_g$  predictions for the Hibiki experiments with the Sugrue model, adjusted Sugrue model, and  $Wo_{new}$  model are shown in Figures 4-1 - 4-4. The adjusted Sugrue model or the  $Wo_{new}$  model perfectly captures the experimental  $\alpha_g$  profiles for every case. Besides 3\_1, 3\_2, and 4\_1 the adjusted Sugrue model captures the general trend for each case. Experiments 3\_1 and 3\_2 may not be fully developed, see Appendix D, and missing these cases is not considered a major concern. For experiment 4\_1 the predicted  $C_L$  is negative in the bulk but becomes slightly positive near the wall, where  $d_b$  is very small. This is the source of the small near-wall peak in  $\alpha_g$ , but still the general trend is captured. While not perfect, the adjusted Sugrue model results in a lower MAE in  $\alpha_g$  than the original Sugrue formulation.

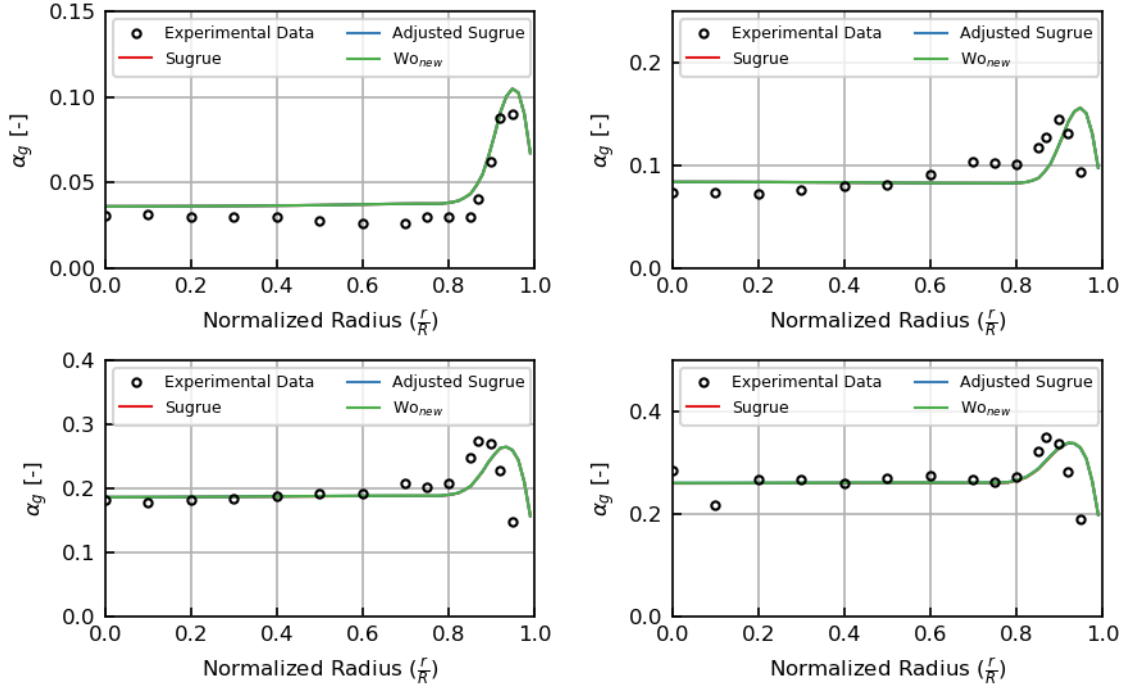


**Figure 4-1:** Comparison of  $\alpha_g$  profiles from Sugrue, the adjusted Sugrue, and  $W_{o_{new}}$  on Hibiki 1\_1 (top left), 1\_2 (top right), 1\_3 (bottom left), and 1\_4 (bottom right)

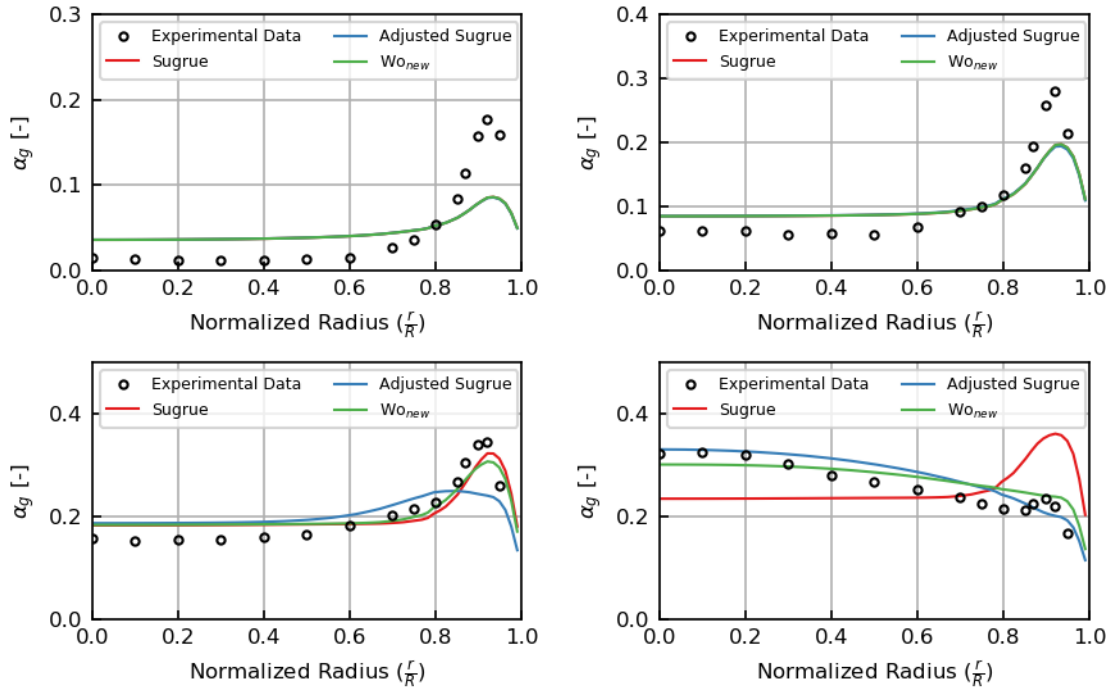


**Figure 4-2:** Comparison of  $\alpha_g$  profiles from Sugrue, the adjusted Sugrue, and  $W_{o_{new}}$  on Hibiki 2\_1 (top left), 2\_2 (top right), 2\_3 (bottom left), and 2\_4 (bottom right)

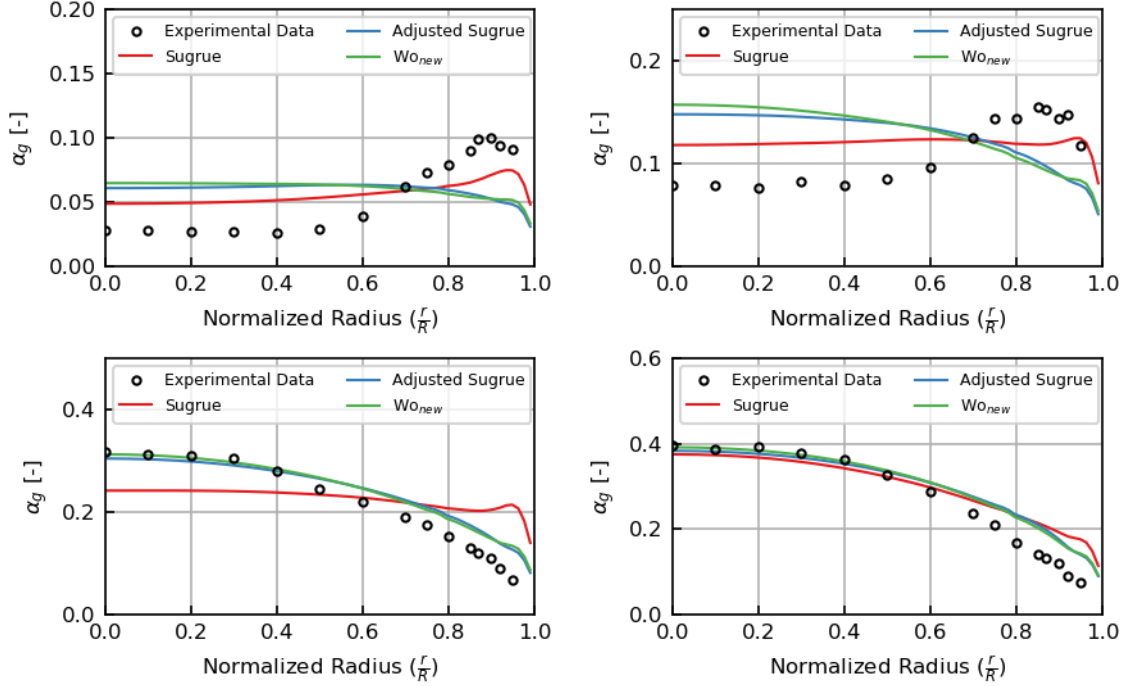


**Figure 4-3:** Comparison of  $\alpha_g$  profiles from Sugrue, the adjusted Sugrue, and  $Wo_{new}$  on Hibiki 3\_1 (top left), 3\_2 (top right), 3\_3 (bottom left), and 3\_4 (bottom right)

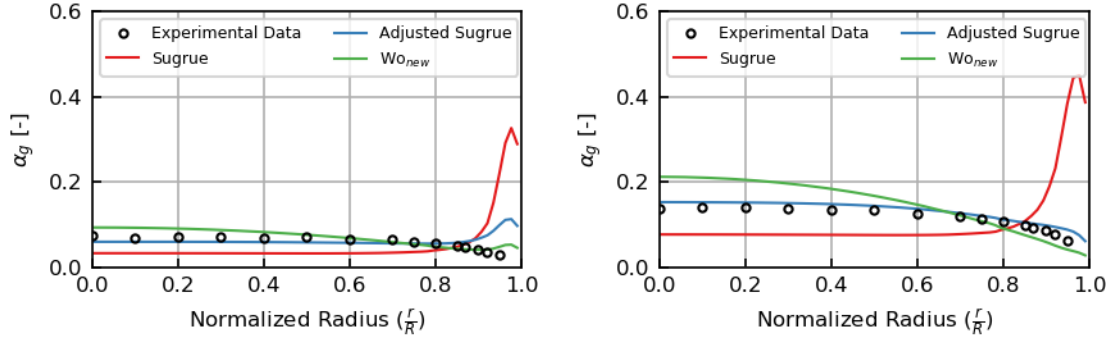


**Figure 4-4:** Comparison of  $\alpha_g$  profiles from Sugrue, the adjusted Sugrue, and  $Wo_{new}$  on Hibiki 4\_1 (left) and 4\_2 (right)

The  $Wo_{new}$  model only misses the general trend for experiments 3\_1 and 3\_2 which again may not be fully developed (see Appendix D). This means that the new model is able to correctly predict the general trend in  $C_L$  across all of the fully developed Hibiki cases. This is a strong improvement over the previous formulation, and provides support that the new formulation is more robust and physically consistent. For both models, the cap of  $C_L$  at 0.03 is too low to capture the size of the wall-peaks in  $\alpha_g$  for

cases 2\_1 and 2\_2 but it captures the magnitude of  $C_L$  for cases 1\_1 - 1\_4 well, thus no adjustments were made. Both models appear to out-perform the original Sugrue model on prediction of  $\alpha_g$ . See Appendix B for the resulting  $U_l$  and  $U_g$  profiles.

A qualitative comparison of the models is performed in Figure 4-5 which is a spread error plot. In Figure 4-5 the x-axis is the experimental value at each measurement point while the y-axis is the M-CFD value at the same points. A point on the  $y = x$  line means the two values are exactly equal, while the dotted lines represent an absolute  $\alpha_g$  margin of  $\pm 10\%$ . Additionally the MAE for each model across the entire Hibiki experiment is compared in the legend. The adjusted Sugrue model has the lowest error followed by the  $Wo_{new}$ , then the Sugrue model. Both new models out-perform the original Sugrue model on predicting the general trend in  $C_L$ , accomplishing Objective 1 of this thesis.

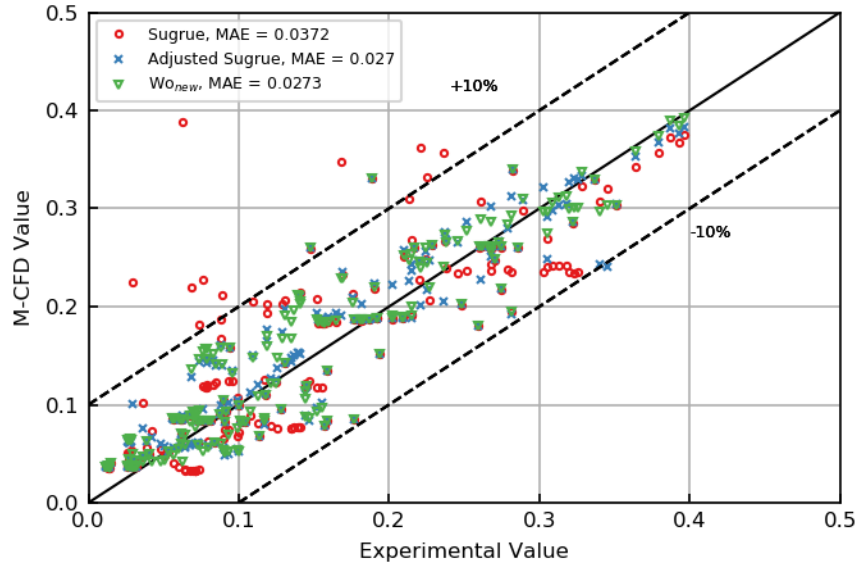


**Figure 4-5:** Spread error on  $\alpha_g$  profiles from Sugrue, the adjusted Sugrue, and  $Wo_{new}$  on Hibiki experiment

## 4.2 Developing Flow

The TOPFLOW experiment was able to highlight challenges for the original Sugrue model, so it was selected for validation of the newly proposed models. The

TOPFLOW experiment provides multiple measurements at varying distances from the injection location, in order to assess the flow development. Air is injected at the pipe wall, which allows for a clear study of the  $\alpha_g$  migration to the pipe center due to a negative  $C_L$ . A more detailed description of the TOPFLOW experiment and the simulation set up can be found in Appendix C. The resulting  $\alpha_g$  predictions on the TOPFLOW experiments for the Sugrue model, adjusted Sugrue model, and  $Wo_{new}$  model are shown in Figures 4-6 - 4-9.

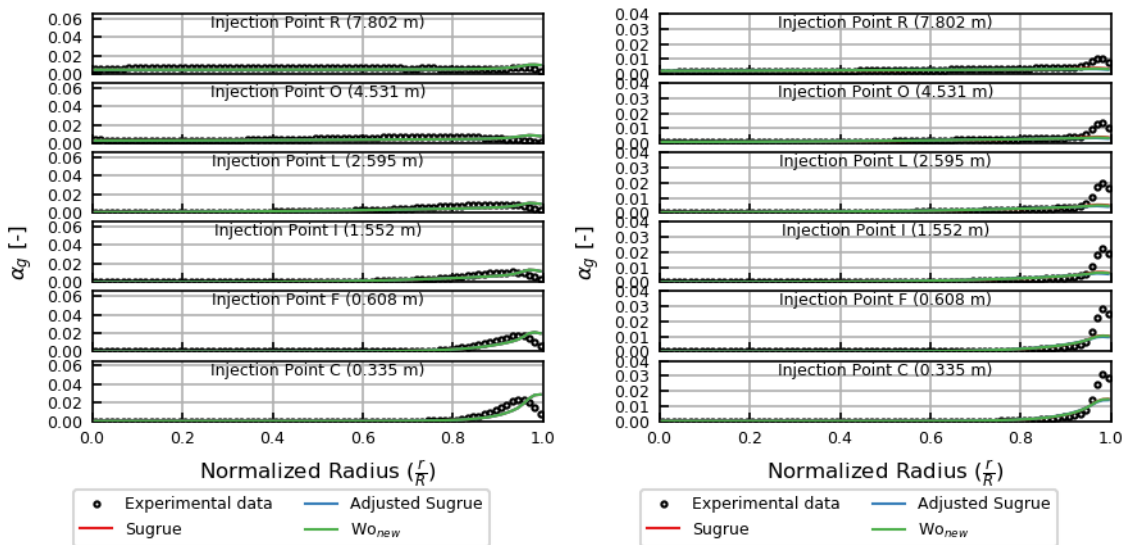


**Figure 4-6:** Comparison of  $\alpha_g$  profiles from Sugrue, the adjusted Sugrue, and  $Wo_{new}$  on TOPFLOW 006 (left) and 008 (right)

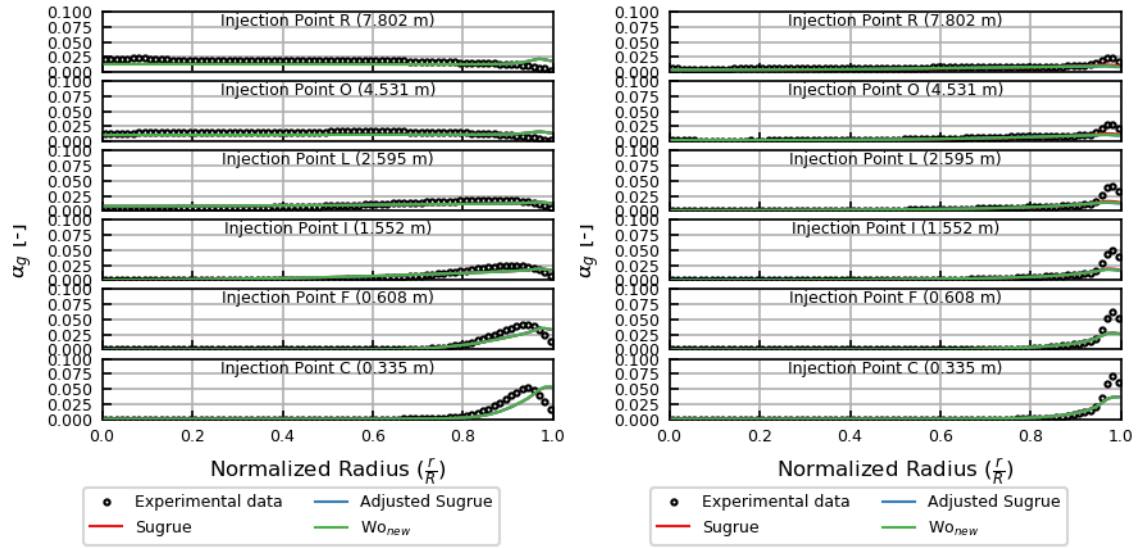


**Figure 4-7:** Comparison of  $\alpha_g$  profiles from Sugrue, the adjusted Sugrue, and  $Wo_{new}$  on TOPFLOW 028 (left) and 030 (right)

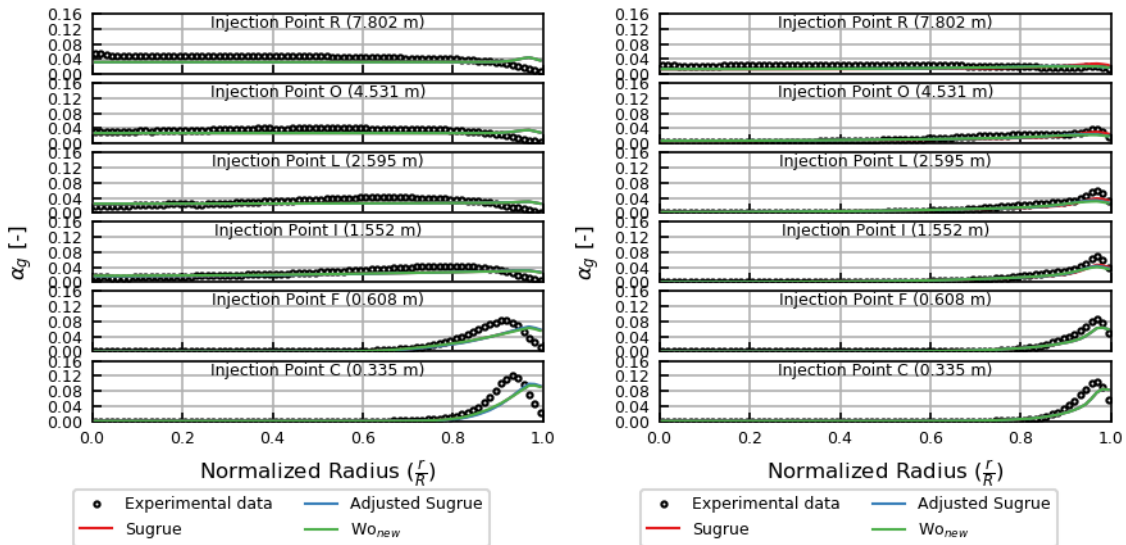


**Figure 4-8:** Comparison of  $\alpha_g$  profiles from Sugrue, the adjusted Sugrue, and  $Wo_{new}$  on TOPFLOW 050 (left) and 052 (right)

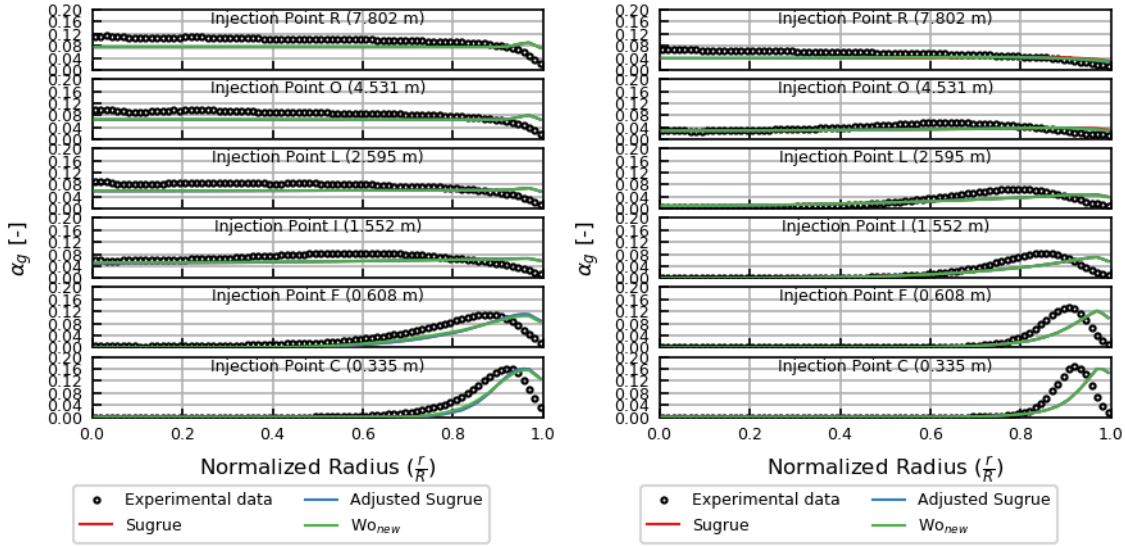


**Figure 4-9:** Comparison of  $\alpha_g$  profiles from Sugrue, the adjusted Sugrue, and  $Wo_{new}$  on TOPFLOW 072 (left) and 074 (right)

The models do not appear to perform very differently on TOPFLOW. See Appendix C for the resulting  $U_l$  and  $U_g$  profiles. A qualitative comparison of the models is shown using a spread error plot in Figure 4-10. Near-wall  $\alpha_g$  peaks are still incorrectly predicted for cases 028, 050, 072 from all three models. Meanwhile for cases 008 and 030 a wall-peak is observed experimentally but is not predicted by any of the models. The  $Wo_{new}$  model has very marginally improved results on the TOPFLOW experiment when compared to the Sugrue model. Meanwhile the adjusted Sugrue model performs identically to the Sugrue model. This suggests that that only shifting the lift inversion using the same  $Wo$  is not sufficient to correctly predict the lift inversion on TOPFLOW with the selected models.

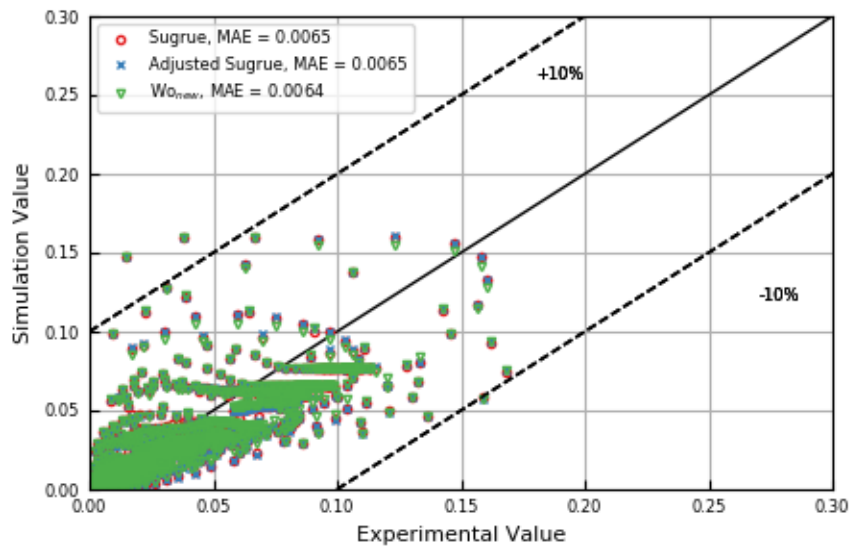


**Figure 4-10:** Spread error on  $\alpha_g$  profiles from Sugrue, the adjusted Sugrue, and  $Wo_{new}$  on TOPFLOW experiment



# Chapter 5

## Machine Learning For Data Analysis

The second objective for this thesis is to take the data generated in Chapter 3 and to leverage advanced data processing tools to probe for additional physics information. The candidate methods are k-nearest neighbors (k-NN), principal component analysis (PCA), linear regression, random forests, and neural networks. The goal for these methods is to test their ability to provide the best predictions of  $C_L$  and/or be leveraged to infer variable importance from the data. These methods are not meant to replace the model development process but to provide insights for future modeling efforts. It is assumed that these M-CFD simulations are physically consistent therefore allowing them to sample from a distribution very similar to real world physics.

Section 5.1 provides a brief background on each of the candidate models. The methods used for this analysis are detailed in Section 5.2. The final  $C_L$  predictions and variable importance information are presented in Section 5.3.

### 5.1 Machine Learning Background

#### 5.1.1 k-NN

k-NN is the simplest method applied, it requires no model [25]. Instead, k-NN makes prediction on new data based on the  $k$  nearest data points from the training data.

The distance between data points is typically calculated as classic Euclidean distance or the distance between the points as measured along the axes at right angles ("Manhattan" distance). Since regression from k-NN does not create a model, there is no way to process out variable importance. However, if k-NN trained on M-CFD data can make accurate predictions on experimental data then the assumption that the two sets of data come from a very similar distribution is supported. Variable parameters for this method include the distance function, number of points each example is compared to, and how neighboring points are weighted (uniformly or scaled by distance) [25, 26].

### 5.1.2 Principal Component Analysis

Principal component analysis is a data reduction technique. The data is reduced from the input variables into principal components which are orthogonal, linear combinations of the original variables. Each successive component spans the maximum possible variance from the original data. As more principal components are taken, more of the variance of the original data is recovered. The only variable parameter for this method is the number of principal components that the data is reduced down to (e.g. two components) [26, 27].

### 5.1.3 Linear Regression

Linear regression solves for the linear combination of the input parameters which minimizes the squared distance between the generated line and each data point. Linear regression can be regularized by penalizing using more variables (L1), penalizing higher absolute values for parameter coefficients (L2), or a combination of the two. The final objective function ( $J$ ) is

$$J(Y|X, w) = \frac{1}{2n_{samples}} \|Y - X \bullet w\|^2 + \lambda_{L1} \|w\|_1 + \lambda_{L2} \|w\|^2 \quad (5.1)$$

where  $Y$  is a matrix (or vector) of the actual values,  $X$  is a matrix of the input data,  $n_{samples}$  is the number of data points, and  $w$  is the weight vector of the regression

coefficients. Variable parameters for this method include  $\lambda_{L1}$  and  $\lambda_{L2}$  values [28, 26].

#### 5.1.4 Random Forests

Random forests use a collection of decision trees to make a prediction which can be a classification or a discrete value. Each decision tree in the forest is given a random subset of the input variables to use. With these variables, the decision tree makes splits in the data based off the input data until reaching a final prediction. The results from all of the trees are then averaged to obtain the prediction value for the forest [29, 30]. Random forests do not have as many hyper-parameters that require tuning as neural networks do, but can represent more complex relationships than linear regression. Variable parameters include the number of trees, the number of samples for a decision boundary, the number of decisions per tree, and the minimum error decrease for a decision. Additionally, random forests provide a clear interpretation of variable importance based off how many times a variable is used for a decision boundary within the forest [26].

#### 5.1.5 Neural Networks

Neural networks consist of successive weight matrices multiplied by incoming data, the result of which is then put through a non-linear activation functions and passed to the next layer. Their architecture consists of an: input layer, hidden layer(s), and an output layer. Connections between layers can vary, a common approach is to have each node in a layer connected to every node in the previous layer, this is known as fully connected or dense layers. For this work, dense layers are being used in a feedforward network. Dropout [31] along with regularization in the loss function can prevent over-fitting. The downsides of neural networks for this application is that they do not provide any clear information about how variables are being used and that they require a large amount of data to train. Therefore little future modeling information is directly gained from just fitting one network.

## 5.2 Leveraging Machine Learning as a Data Analysis Tool

### 5.2.1 Data Flow

15 local flow parameters of interest were taken from the M-CFD data created during the  $C_L$  optimization on the Hibiki experiment. The selected variables were:  $\alpha_g, U_l, U_g, d_b, \alpha_g^2, U_l^2, U_g^2, d_b^2, J_l, J_g, S, \frac{\partial \alpha_g}{\partial r}, \frac{\partial U_l}{\partial r}, \frac{\partial U_g}{\partial r}$ , and  $\frac{\partial d_b}{\partial r}$ . These include the liquid superficial velocity ( $J_l = \frac{U_l}{1-\alpha_g}$ ), gas superficial velocity ( $J_g = \frac{U_g}{\alpha_g}$ ), and slip ratio ( $S = \frac{U_l}{U_g}$ ), along with the partial derivatives with respect to radial position of  $\alpha_g, U_l, U_g$ , and  $d_b$ . To ensure reliable predictions could be made across the M-CFD optimization data and the experimental data the two data sets were combined and each variable value ( $x$ ) was z-scaled,

$$z = \frac{x - \mu}{\sigma} \quad (5.2)$$

where  $\mu$  is the average value and  $\sigma$  is the standard deviation, then the two data sets were separated.

The M-CFD data was randomly shuffled, then 90% of the data was taken out for model testing and hyper-parameter tuning ( $X$  for the flow parameters  $Y$  for the  $C_L$  values). hyper-parameter tuning and model training was performed via a 5-fold cross-validation using the GridSearchCV method from scikit-learn predicting  $Y$  from  $X$  [26]. The validation error was then calculated using the remaining 10% of the M-CFD data ( $X_V$  for the flow parameters  $Y_V$  for the  $C_L$  values), making predictions from  $X_V$  ( $Y_{CFD}$ ) and comparing them to  $Y_V$ . Experimental predictions for  $C_L$  ( $Y_{exp}$ ) were then made from the experimental flow parameters ( $X_{exp}$ ). The experimental error was calculated by comparing  $Y_{exp}$  to the human analysis values of  $C_L$  from Chapter 4 ( $Y_{human}$ ). Since the values for  $C_L$  are all  $< |1|$  the mean absolute error (MAE) was used as the error in all cases and settings.

To summarize:

1. The  $X, X_v$ , and  $X_{exp}$  datasets were jointly z-scaled

2. A 5-fold cross-validation was performed for each of the selected models using  $X$  and  $Y$  to train the models and tune their hyper-parameters.
3.  $Y_{CFD}$  was calculated from predictions on  $X_V$ .
4. Validation error was calculated as the MAE between  $Y_{CFD}$  and  $Y_V$ .
5.  $Y_{exp}$  was calculated from predictions on  $X_{exp}$ .
6. Experimental error was calculated as the MAE between  $Y_{exp}$  and  $Y_{human}$ .

The resulting validation errors,  $Y_{exp}$ , and experimental error are presented in Section 5.3.

### 5.2.2 Method Settings

All of the machine learning models were implemented in Python v3.7.4. Data was read in and processed using Pandas v0.25.1 data frames and Numpy v1.16.5 arrays. The k-NN, PCA, linear regression, and random forests methods were implemented within models from scikit-learn v0.21.3 and hyper-parameters were tuned using the GridSearchCV method. Neural networks were implemented using Tensorflow v1.14.0. The specific methods and setting for each setting are as follows.

- k-NN: KNeighborsRegressor method,  $n\_neighbors = 5$ ,  $metric = \text{minkowski}$ ,  $p = 1$ ,  $weights = \text{'distance'}$
- PCA: PCA method,  $n\_components = 2$
- Linear regression: linear\\_model ElasticNet method,  $alpha = 0.2$ ,  $fit\_intercept = \text{False}$ ,  $l1 \text{ ratio} = 0.1$
- Random forest: ensemble RandomForestRegressor method,  $n\_estimators = 1000$ ,  $max\_depth = 100$ ,  $min\_impurity\_decrease = 0.01$ ,  $min\_samples\_leaf = 5$ .

- Neural network: Keras Dense Layers method, 1 hidden layer with 20 nodes, Rectified Linear Unit (ReLU) activation, learning\_rate = 0.0003, dropout = 0.01, batch\_size = 30, optimizer = tf.keras.optimizers.Adam, loss = MAE, metrics = MAE, epochs = 5000, validation\_split = 0.2, callbacks = [EarlyStopping (monitor = 'val\_loss', min\_delta = 1E-7, patience = 100, restore\_best\_weights = True)]

### 5.2.3 Variable Importance Calculations

Variable importance was calculated similarly for each method. The variable importance for linear regression, random forests, and PCA were calculated by taking the magnitude of the coefficients, variable importance, and components, respectively, for each variable across all 15 positions as a vector. A higher absolute value for linear regression coefficient corresponds to a greater contribution to the model. A higher value of variable importance from the decision tree variable importance corresponds to a variable the model used more. A higher absolute value of the component coefficient for the first principle component corresponds to the variable contributing more to the vector which spans the most variance of the data. The variables were then sorted by the L2, vector norm (or length) of the resulting vectors.

The k-NN algorithm does not provide details on variable usage or importance so no variable importance was calculated. Neural networks do not provide clear details on variable usage or variable importance. Therefore these two methods are not used to study variable importance. The calculated importances are compared in Section 5.3.

## 5.3 Insights for Lift Modeling from Machine Learning

The resulting MAE on the validation M-CFD data ( $X_V$  and  $Y_V$ ) for the k-NN, linear regression, random forest, and neural network methods were 0.0004, 0.0298, 0.0261,

and 0.0013 respectively. The resulting experimental  $C_L$  predictions are shown in Figure 5-1 and Table 5.1. The error between  $Y_{exp}$  and  $Y_{human}$  for the k-NN, linear regression, random forest, and neural network methods were 0.0104, 0.0199, 0.0262, 0.2015 respectively. The k-NN algorithm performed the best on both the validation data and experimental  $C_L$  predictions. The neural network performed the second best on the validation data and the worst on the experimental data. Meanwhile the linear regression and random forest alternated in performance from the validation data to the experimental data.

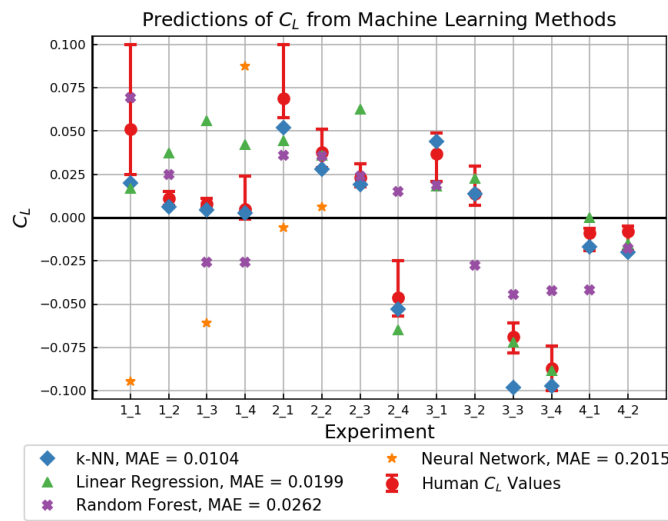


**Figure 5-1:** Comparison of  $C_L$  predictions from machine learning methods to the human analysis

**Table 5.1:** Tabulated  $C_L$  values from k-NN, linear regression (LR), random forest (RF), and neural networks (NN) machine learning methods

Experiment	$C_L$ prediction				
	Human	k-NN	LR	RF	NN
1_1	0.051	0.020	0.017	0.050	-0.095
1_2	0.011	0.006	0.037	0.050	0.197
1_3	0.008	0.004	0.056	-0.023	-0.061
1_4	0.005	0.003	0.042	-0.023	0.088
2_1	0.069	0.052	0.044	0.050	-0.006
2_2	0.038	0.028	0.036	0.050	0.006

<b>2_3</b>	0.023	0.019	0.063	0.050	-0.154
<b>2_4</b>	-0.046	-0.053	-0.065	0.042	0.434
<b>3_1</b>	0.037	0.044	0.018	0.050	-0.304
<b>3_2</b>	0.014	0.014	0.022	-0.042	-0.165
<b>3_3</b>	-0.069	-0.098	-0.072	-0.050	-0.118
<b>3_4</b>	-0.087	-0.097	-0.088	-0.050	-0.259
<b>4_1</b>	-0.009	-0.017	0.000	-0.050	-0.41
<b>4_2</b>	-0.008	-0.020	-0.015	-0.050	-0.439

It was surprising to find that the linear regression out performed the random forest and neural network on the experimental predictions. One explanation could be that the linear regression model was much more regularized then the random forest and neural network. It was observed that better tuning the `min_impurity_decrease` and `min_samples_leaf` parameters could have been used to regularize the random forest models, which may have boosted the model performance.

A higher dropout could have improved the regularization of the network. Adding an L2 or L1 value into the loss function also could have regularized the network by limiting the magnitude of network coefficients and nodes used respectively. Due to the length of time it took to train the random forests and neural networks they were not tuned as much as desired. Especially because the architecture and hyper-parameters for the neural network create a huge array of settings to test.

Another potential source of error for the neural network could have been that it was over fit to the M-CFD data. However looking at the training losses in Figure 5-2, it appears the early stopping prevented the model from over fitting since the validation loss had not started increasing. The most likely reason that the random forest and neural networks methods performed poorly is that there were not enough data points to adequately train either method. The validation loss being lower than the training



loss in 5-2 may be a supporting sign that there is too little data to fit a neural network.

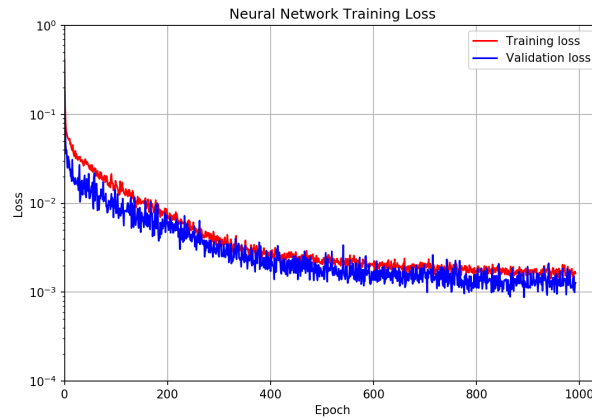


**Figure 5-2:** Training and validation errors for the neural network

The k-NN algorithm performed the best, but carries no variable importance information, which ultimately does not further the goal for this project. It does lend evidence to support the assumption that the M-CFD simulations are physically consistent enough that they sample from a distribution very similar to real world physics. The linear regression does correctly predict the sign of  $C_L$  which is promising.

The calculated feature importances from linear regression, random forests, and PCA as detailed in Section 5.2.3 are shown in Figure 5-3. The importances are normalized so that an importance of sixteen indicates the most important variable from the calculation for the respective method while an importance on one is the least important variable.

The linear regression and random forest methods both suggest that  $J_l$ ,  $J_g$ , and  $S$  are the three most important variables. Meanwhile PCA suggests that  $\frac{\partial \alpha_g}{\partial r}$ ,  $d_b^2$ , and  $\alpha_g$  are the three most important variable. However since linear regression did correctly predict the sign of  $C_L$  for each case, its results are the ones given the most consideration. This is further supported by the agreement with the random forest, but the physical interpretation of a local superficial velocity is not clear. Leveraging these

data analysis tools will likely require more data and further study than performed in this work to get meaningful information for future modeling efforts.

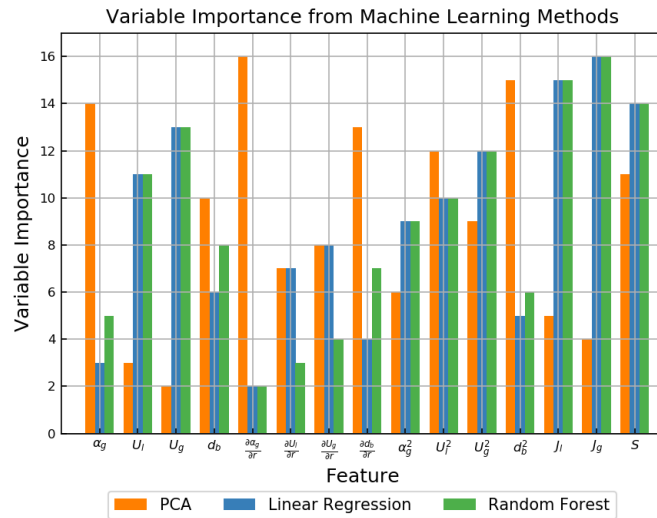


**Figure 5-3:** Comparison of variable importances from linear regression, random forest, and PCA

# Chapter 6

## Conclusions and Future Work

An adjustment to the Sugrue model has been proposed, along with a new turbulent lift model leveraging the proposed  $Wo_{new}$ , utilizing a numerical optimization of  $C_L$  on the Hibiki experiment. Both models out perform the original Sugrue model when simulating the Hibiki experiment. Both models perform better at capturing the general trend in  $C_L$  observed in the Hibiki experiment, which previous models could not reproduce. On the TOPFLOW experiment, the  $Wo_{new}$  model performs marginally better than the adjusted Sugrue, which performs identically to the Sugrue model. Based off the overall model performance  $Wo_{new}$  is recommended since it: outperforms the original Sugrue model, predicts the right  $\alpha_g$  peak location for all of the fully developed Hibiki experiments, performs slightly better on the validation experiment, and has a formulation more conducive for future modeling. The  $Wo_{new}$  model is more accurate and generally applicable than the original Sugrue model, accomplishing the first objective for this thesis.

The new model still fails to correctly predict the lift inversion for the TOPFLOW experiment. Since there are no liquid turbulence measures for the TOPFLOW experiment it is hard to know if the turbulence solution is correct. Turbulence is clearly an important factor for modeling  $C_L$  accurately, and incorrect turbulence may be the key to why the lift inversion is missed. A BIT model may be necessary to accurately model lift inversion for the TOPFLOW experiment. But even with a BIT model the

results would still be difficult to validate without experimental turbulence measures.

While it is difficult to obtain detailed data for both the liquid phase (e.g. turbulence quantities) and for the gas phase (e.g. bubble size distributions) they are necessary for the development of robust M-CFD models. Further study of the lift force would benefit from optimization of  $C_L$  on experiments with high quality data for both phases. This would provide more points for modeling  $C_L$  and avenues for additional insights on how to model the lift inversion. The limit for this is the lack of high quality, CFD-grade experiments similar to the TOPFLOW data.

For future study of lift modeling, a correlation which is valid for both laminar and turbulent conditions could be created using a term similar to  $Wo_{new}$ . This would further advance the understanding of how the continuous phase turbulence affects bubble migration and shape. This could lead to improved models for interfacial area density along with other momentum closures like turbulent dispersion and drag. DNS data may be further leveraged to better understand the complex interactions between all of these forces.

Candidate machine learning models: k-NN, PCA, linear regression, random forests, and neural networks, were leveraged to further study the Hibiki  $C_L$  optimization data. Between k-NN, linear regression, random forests, and neural networks, k-NN made the best predictions of  $C_L$  on validation data and the experimental data. This provides support for the assumption that the M-CFD data and real world physics sample from the same distribution. It does not provide any information for future modeling efforts.

PCA, linear regression, and random forests were also utilized to study variable importance. The importances from linear regression may be the most useful since that model was able to accurately predict the sign of  $C_L$  for each case. The fact that the random forest provide the same rankings is promising, even though the predictions

from the random forest were not as strong. The variable importance study suggests that  $J_l$ ,  $J_g$ , and  $S$  are the three most important variables for modeling  $C_L$ .

The sign change in  $C_L$  has a physical meaning (lift inversion) and correct modeling of this phenomena is crucial. Therefore it is very encouraging that the k-NN and linear regression methods do well in predicting the sign of the lift coefficient from the experimental data. It was expected that the physics on hand would be highly non-linear, but the overall performance of the these two models using just squared terms suggests the underlying physics may be simpler than expected. With more time and parameter exploration for each of the models, its possible that a data driven analysis could uncover some physical insights. However, the current results do not show much clear information about parameters for use in modeling and do not provide much physical insight in their current state. This takes a step in the direction of the second objective for this thesis, but does not achieve it.

For future study using machine learning to gain modeling insights, it is believed that there would be a great value added by increasing the amount of M-CFD data to train with. With the current data, only 2,533 samples were actually used for the cross-validation to select hyper-parameters and train the model. Additional data could be generated by changing the model or value for another momentum closure force, e.g. the drag force. For the example of the drag force, changing it would also increase the variation of the M-CFD  $U_g$  values, which could then better capture the range of  $U_g$  values seen in the experimental data. This would not only increase the amount of available data, but it would also increase how representative the M-CFD data is of the experimental data. Since the lift force is directly proportional to the relative velocity between the phases, as drag decreases a smaller  $C_L$  also has a larger effect on  $\alpha_g$ . The downside of doing this is that its a slow process, each re-run of all the lift values would take roughly a month on the currently available computational resources.



# Bibliography

- [1] G. Yeoh and J. Tu, *Computational Techniques for Multiphase Flows – Basics and Applications*. Oxford UK: Butterworth-Heinemann, 2010.
- [2] J. Lu and G. Tryggvason, “Effect of bubble deformability in turbulent bubbly upflow in a vertical channel,” *Physics of Fluids*, vol. 20, 2008.
- [3] R. Sugrue, *A Robust Momentum Closure Approach for Multiphase Computational Fluid Dynamics Applications*. PhD thesis, Massachusetts Institute of Technology, Cambridge, MA, 2017.
- [4] M. Shiea, A. Buffo, E. Baglietto, D. Lucas, M. Vanni, and D. Marchisio, “Evaluation of hydrodynamic closures for bubbly flow regime cfd simulations in developing pipe flow,” *Chemical Engineering and Technology*, 2019.
- [5] B. Casel and E. Baglietto, “Assessment of MIT momentum closure relations for developing, bubbly flow regimes,” (Portland, OR), American Nuclear Society, NURETH-18, 2019.
- [6] T. Hibiki, M. Ishii, and Z. Xiao, “Axial interfacial area transport of vertical bubbly flows,” *International Journal of Heat and Mass Transfer*, vol. 44, pp. 1869–1888, 7 2001.
- [7] M. Beyer, D. Lucas, J. Kussin, and P. Schutz, “Air-water experiments in a vertical DN200-pipe,” Tech. Rep. FZD-505, Helmholtz-Zentrum Dresden-Rossendorf, Dresden, Germany, 2008.
- [8] A. Tomiyama, H. Tamai, I. Zun, and S. Hosokawa, “Transverse migration of single bubbles in a simple shear flows,” *Chemical Engineering Science*, vol. 57, pp. 1849–1858, 2002.
- [9] R. Kommajosyula, G. Bois, A. Burlot, M.-G. Rodio, B. Cariteau, and E. Baglietto, “A criterion to classify void fraction profiles in adiabatic bubbly flows based on averaged flow quantities for use in subchannel codes,” (Portland, OR), American Nuclear Society, NURETH-18, 2019.
- [10] A. U. M. Masuk, A. Salibindla, S. Tan, and R. Ni, “V-onset (vertical octagonal noncorrosive stirred energetic turbulence): A vertical water tunnel with a large energy dissipation rate to study bubble/droplet deformation and breakup

- in strong turbulence,” *Review of Scientific Instruments*, vol. 90, no. 8, p. 085105, 2019.
- [11] P. Saffman, “The lift on a small sphere in a slow shear flow,” *Journal of Fluid Mechanics*, vol. 22, pp. 385–400, 1965.
- [12] T. Auton, “The lift force on a spherical body in a rotational flow,” *Journal of Fluid Mechanics*, vol. 183, pp. 199–218, 1987.
- [13] J. McLaughlin, “Inertial migration of small sphere in linear shear flows,” *Journal of Fluid Mechanics*, vol. 224, pp. 261–274, 1991.
- [14] T. Hibiki and M. Ishii, “Lift force in bubbly flow systems,” *Chemical Engineering Science*, vol. 62, no. 22, pp. 6457–6474, 2007.
- [15] D. Legendre and J. Magnaudet, “The lift force on a spherical bubble in a viscous linear shear flow,” *Journal of Fluid Mechanics*, vol. 368, pp. 81–126, 1998.
- [16] W. Dijkhuizen, M. Annaland, and J. Kuipers, “Numerical and experimental investigation of the lift force on single bubbles,” *Chemical Engineering Science*, vol. 65, no. 3, pp. 1274–1287, 2010.
- [17] N. Lubchenko, B. Magolan, R. Sugrue, and E. Baglietto, “A more fundamental wall lubrication force from turbulent dispersion regularization for multiphase cfd applications,” *International Journal of Multiphase Flow*, pp. 46–44, 2004.
- [18] A. Burns, T. Frank, I. Hamill, and J.-M. Shi, “The Farve averaged drag model for turbulent dispersion in Eulerian multi-phase flows,” (Yokohama, Japan), 5th International Conference on Multiphase Flow, 2004.
- [19] M. Colombo and M. Fairweather, “Multiphase turbulence in bubbly flows: Rans simulations,” *International Journal of Multiphase Flow*, vol. 77, pp. 222–243, 2015.
- [20] E. Baglietto and M. Christon, “Demonstration & assessment of advanced modeling capabilities to multiphase flow with sub-cooled boiling,” Tech. Rep. CASL-U 2013-0181-001, CASL, 2013.
- [21] S. Kriebitzsch and R. Rzehak, “Baseline model for bubbly flows: simulation of monodisperse flow in pipes of different diameters,” *Fluids*, vol. 29, 2016.
- [22] D. Lucas and A. Tomiyama, “On the role of the lateral lift force in poly-dispersed bubbly flows,” *International Journal of Multiphase Flow*, vol. 37, no. 9, pp. 1178–1190, 2011.
- [23] R. Sugrue, B. Magolan, N. Lubchenko, and E. Baglietto, “Assessment of a simplified set of momentum closure relations for low volume fraction regimes in STAR-CCM+ and OpenFOAM,” *Annals of Nuclear Energy*, vol. 110, pp. 79–87, 2017.



- [24] B. Magolan, *Extending Bubble-Induced Turbulence Modeling Applicability in CFD through Incorporation of DNS Understanding*. PhD thesis, Massachusetts Institute of Technology, Cambridge, MA, 2018.
- [25] S. Dudani, “The distance-weighted k-nearest-neighbor rule,” *IEEE Transactions on Systems, Man, and Cybernetics*, vol. SMC-6, no. 4, 1976.
- [26] F. Pedregosa, G. Varoquaux, A. Gramfort, V. Michel, B. Thirion, O. Grisel, M. Blondel, P. Prettenhofer, R. Weiss, V. Dubourg, J. Vanderplas, A. Passos, D. Cournapeau, M. Brucher, M. Perrot, and E. Duchesnay, “Scikit-learn: Machine learning in Python,” *Journal of Machine Learning Research*, vol. 12, pp. 2825–2830, 2011.
- [27] S. Wold, K. Esbensen, and P. Geladi, “Principal component analysis,” *Chemometrics and Intelligent Laboratory Systems*, vol. 4, no. 1-3, pp. 37–52, 1987.
- [28] J. Friedman, T. Hastie, and R. Tibshirani, “Regularization paths for generalized linear models via coordinate descent,” *Journal of Statistical Software*, vol. 33, 2010.
- [29] L. Breiman, *Machine Learning*. Alphen aan den Rijn, The Netherlands: Kluwer Academic Publishers, 2001.
- [30] T. Ho, “A criterion to classify void fraction profiles in adiabatic bubbly flows based on averaged flow quantities for use in subchannel codes,” (Montreal, Canada), pp. 278–282, IEEE, Proceedings of 3rd International Conference on Document Analysis and Recognition, 1995.
- [31] N. Srivastava, G. Hinton, A. Krizhevsky, I. Sutskever, and R. Salakhutdinov, “Dropout: A simple way to prevent neural networks from overfitting,” *Journal of Machine Learning Research*, vol. 15, pp. 1929–1958, 2014.
- [32] A. Tomiyama, I. Kataoka, I. Zun, and T. Sakaguchi, “Drag coefficients of single bubbles under normal and micro gravity conditions,” *JSME International Journal*, vol. 42, no. 2, pp. 472–479, 1998.
- [33] D. Shaver and M. Podowski, “Modeling of interfacial forces for bubbly flows in subcooled boiling conditions,” (Washington D.C.), American Nuclear Society, Winter Meeting, 2015.



# Appendix A

## Model Implementation in STAR-CCM+

The lift coefficient is implemented through the Podwoski near wall correction. Equation:

$$C_L = \begin{cases} 0 & \frac{y_w}{d_b} < \frac{1}{2} \\ C_{L,0} \left( 3 \left( \frac{2y_w}{d_b} - 1 \right)^2 - 2 \left( \frac{2y_w}{d_b} - 1 \right)^3 \right) & \frac{1}{2} \leq \frac{y_w}{d_b} \leq 1 \\ C_{L,0} & 1 < \frac{y_w}{d_b} \end{cases} \quad (\text{A.1})$$

where  $y_w$  is the wall distance and  $C_{L,0}$  is the lift coefficient predicted from either the adjusted Sugrue or the  $Wo_{new}$  model. STAR-CCM+:

```
CL_Podowski = ($WallDistanceAir / $InteractionLengthScale)
< 1/2? (0) :
(($WallDistanceAir / $InteractionLengthScale) < 1)? ($CL)
(3($WallDistanceAir / $InteractionLengthScale) - 1), 2)
- 2pow((2($WallDistanceAir / $InteractionLengthScale) - 1), 3)) :
($CL))
```

where  $\{CL\}$  is the  $C_L$  value from either the adjusted Sugrue or the  $Wo_{new}$ . The adjusted Sugrue model Equation:

$$C_{L,AdjustedSugrue} = f(Wo)f(\alpha_g) \quad (\text{A.2})$$

$$f(\alpha_g) = \max[0, 1.0154 - 1.0154 \exp(8.0506\alpha_g)] \quad (\text{A.3})$$

$$f(\text{Wo}) = \min(0.03, 1.0795 - 1.1276\text{Wo}^{0.0428}) \quad (\text{A.4})$$

$$\text{Wo} = \text{Eo} \frac{k}{U_r^2}. \quad (\text{A.5})$$

STAR-CCM+:

$$\{\text{CL\_Sugrue}\} = \{\text{Wo\_fct}\} * \{\alpha\_fct\}$$

$$\{\alpha\_fct\} = \max(0, 1.0154 - 0.0154 * \exp(8.0506 * \{\text{VolumeFractionGas}\}))$$

$$\{\text{Wo\_fct}\} = \min(0.03, 1.0781 - 1.1276 * \text{pow}(\{\text{Wo}\}, 0.0428))$$

$$\{\text{Wo}\} = (\{\text{PhasePairEotvosNumberWater-Air}\} * \{\text{TurbulentKineticEnergyWater}\}) / (\max(0.00001, \text{pow}(\{\text{PhasePairSlipVelocityWater-Air}\}[2], 2)))$$

The newly proposed and recommended  $\text{Wo}_{new}$  lift model Equation:

$$C_{L, \text{Wo}_{new}} = f(\text{Wo}_{new}) f(\alpha_g) \quad (\text{A.6})$$

$$f(\alpha_g) = \max[0, 1.0154 - 1.0154 \exp(8.0506\alpha_g)] \quad (\text{A.7})$$

$$f(\text{Wo}_{new}) = \min(0.03, \text{Wo}_{new}^{-0.0602} - 0.8391) \quad (\text{A.8})$$

$$\text{Wo}_{new} = \text{Eo} \left(1 + \frac{\sqrt{k} U_l}{U_r^2}\right)^{1.5}. \quad (\text{A.9})$$

STAR-CCM+:

$$\{\text{CL\_Wo\_new}\} = \{\text{Wo\_new\_fct}\} * \{\alpha\_fct\}$$

$$\{\alpha\_fct\} = \max(0, 1.0154 - 0.0154 * \exp(8.0506 * \{\text{VolumeFractionGas}\}))$$

```

$$\text{\$}\{Wo\_new\_fct\} = \min(0.03, \text{pow}(\max(\text{\$}\{Wo\_New\}, 0.0001), -0.0602) - 0.8391)$$

```

```

$$\text{\$}\{Wo\_New\} = \text{\$}\{PhasePairEotvosNumberWater-Air\} * \text{pow}((1 + (\text{pow}(\text{\$}\{TurbulentKineticEnergyWater\}, 0.5) * \text{\$}\{VelocityWater\}^2)) / \max(0.0001, \text{pow}((\text{\$}\{PhasePairSlipVelocityWater-Air\}^2), 2))), 1.5)$$

```



# Appendix B

## Hibiki Experiment

### B.1 Experimental Description

In the Hibiki experiment, air and water were injected and uniformly mixed at the bottom of a 3 m vertical pipe that was 50.4 mm in diameter. For each experimental condition ran, data was collected at a measurement plane 2.72 m from the flow inlet ( $\frac{z}{D} = 53.5$ ) at 15 axial points from  $\frac{r}{R} = 0 - 0.95$ . The measured experimental data includes time averaged  $\alpha_g$ ,  $U_l$ ,  $U_g$ , and sauter mean bubble diameter ( $d_{32}$ ) distributions from the combination of a double-sensor probe and a hot film probe [6]. 18 different experimental conditions were performed by Hibiki with varying mass flow rates of air and water. 14 of those experimental conditions can be simulated to numerical convergence in M-CFD [3]; the air and water superficial velocities simulated are given in Table B.1 below. These 14 cases contain both wall-peaked and core-peaked  $\alpha_g$  profiles with  $\langle \alpha_g \rangle$  values from 0.049 to 0.259 which was why the Hibiki experiment was selected to model the lift inversion phenomena for turbulent, bubbly flow [3].

**Table B.1:** Summary of Hibiki conditions [6]

<b>Experiment</b>	$J_l$	$J_g$
<b>1_1</b>	0.491	0.0275
<b>1_2</b>	0.491	0.0556
<b>1_3</b>	0.491	0.129
<b>1_4</b>	0.491	0.19
<b>2_1</b>	0.986	0.0473
<b>2_2</b>	0.986	0.113
<b>2_3</b>	0.986	0.242
<b>2_4</b>	0.986	0.321
<b>3_1</b>	2.01	0.103
<b>3_2</b>	2.01	0.226
<b>3_3</b>	2.01	0.471
<b>3_4</b>	2.01	0.624
<b>4_1</b>	5.0	0.245
<b>4_2</b>	5.0	0.518

## B.2 Simulation Set Up

The 14 Hibiki experiments were simulated in STAR-CCM+ v13.06.011 using a quarter pipe geometry with a diameter of 0.0508 m and a length of 3 m. A quarter of the pipe was used to take advantage of symmetry to reduce the number of cells required for improved computational efficiency. The quarter pipe was modeled with uniform  $\alpha_g$ ,  $U_l$ , and  $U_g$  profiles at the inlet to mimic the experimental conditions. The pipe wall was a no-slip velocity condition applied while for the remaining two walls symmetry conditions are adopted. The pipe outlet was set to a pressure outlet at atmospheric pressure.



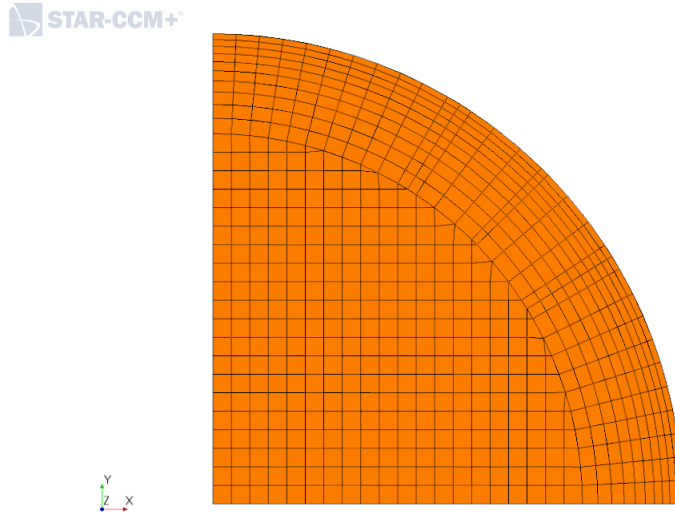


**Figure B-1:** Hibiki computational mesh

The mesh has a base size of 1 mm in the bulk. A total prism layer thickness of 5.4 mm was set with 10 prism layers with a first cell thickness of 0.32 mm. The mesh cells are 10 mm long in the flow wise direction for an aspect ratio of 10. Figure B-1 shows the computational mesh and geometry. The simulations are performed using the experimentally measure sauter mean bubble diameter profiles from the final measurement plane at 2.72 m. This approach allows eliminating potential inaccuracy related to interfacial area predictions, in order to best evaluate the effect of momentum closures. For error calculations, data was taken from the same axial and radial locations as the experimental data.

While values for  $C_L$  were varied for the optimization on the Hibiki experiment and for the validation of the new models, the other momentum closure models in use were kept constant. The models used were consistent with the Bubbly And Moderate void Fraction (BAMF) framework [3, 17, 23]. The models selected are:

1. Turbulence: Standard  $k-\epsilon$  scaled by liquid volume fraction
2. Drag: Tomiyama moderately contaminated drag [32] with no swarm correction
3. Turbulent dispersion: Burns [18]

4. Interfacial area: Experimental sauter mean diameter values

5. Near wall models:

- Turbulence: High  $y^+$  model
- Lift: Podowski near wall correction [33]
- Wall lubrication: Lubchenko [17]

## B.3 Velocity Results

The resulting  $U_l$  profiles for the Sugrue model, adjusted Sugrue model, and  $Wo_{new}$  model are given in Figures B-2 - B-5.

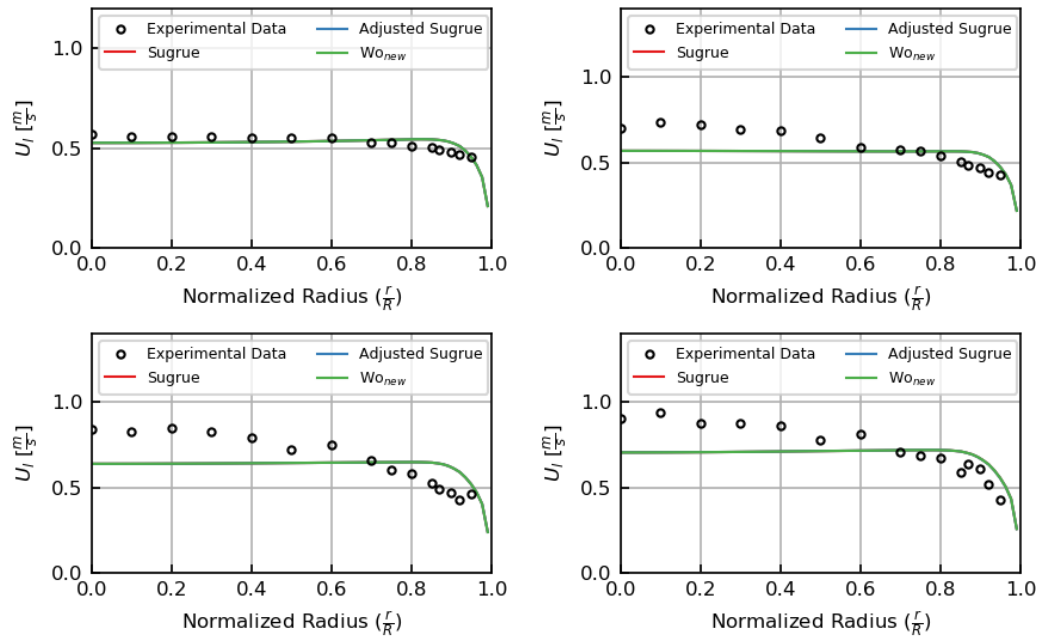


**Figure B-2:** Comparison of  $U_l$  profiles from Sugrue, the adjusted Sugrue, and  $Wo_{new}$  on Hibiki 1\_1 (top left), 1\_2 (top right), 1\_3 (bottom left), and 1\_4 (bottom right)

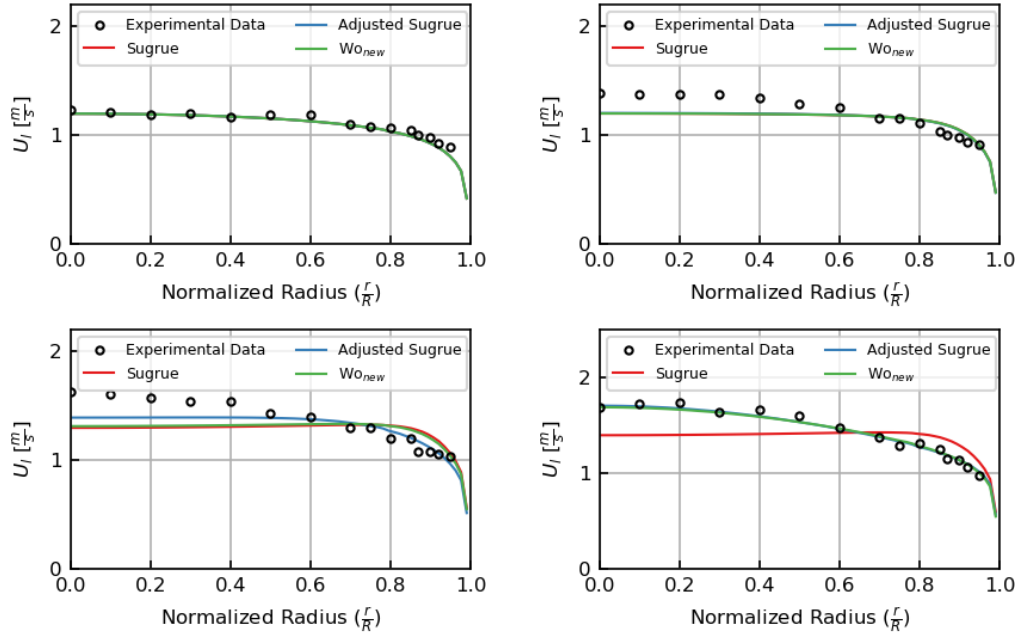


**Figure B-3:** Comparison of  $U_l$  profiles from Sugrue, the adjusted Sugrue, and  $Wo_{new}$  on Hibiki 2\_1 (top left), 2\_2 (top right), 2\_3 (bottom left), and 2\_4 (bottom right)

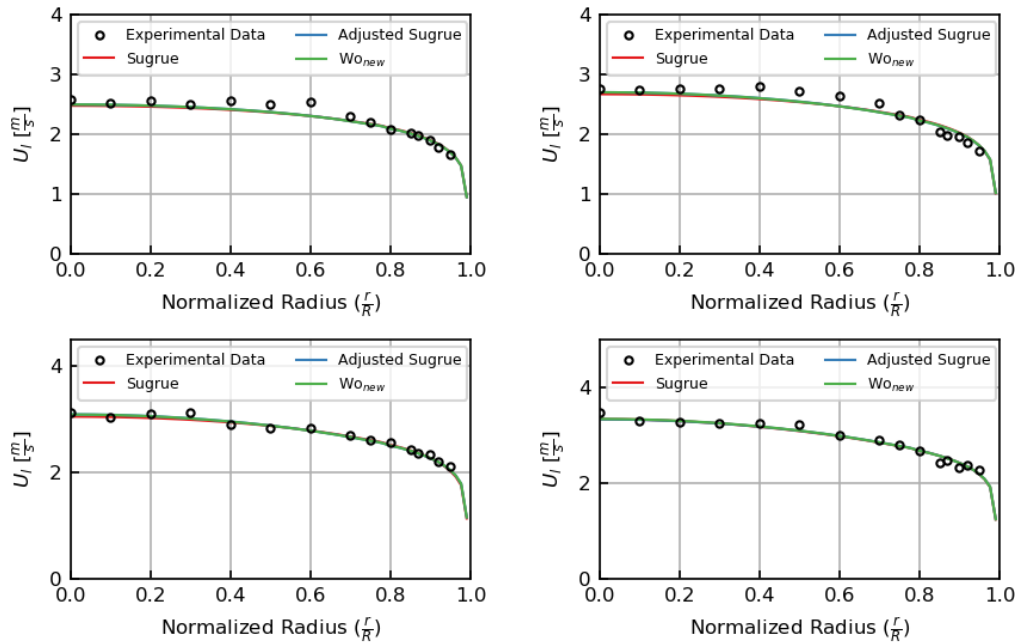


**Figure B-4:** Comparison of  $U_l$  profiles from Sugrue, the adjusted Sugrue, and  $Wo_{new}$  on Hibiki 3\_1 (top left), 3\_2 (top right), 3\_3 (bottom left), and 3\_4 (bottom right)

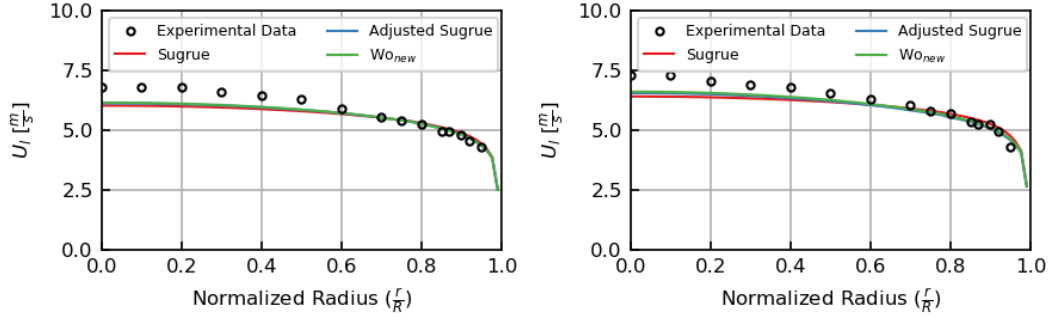


**Figure B-5:** Comparison of  $U_l$  profiles from Sugrue, the adjusted Sugrue, and  $Wo_{new}$  on Hibiki 4\_1 (left) and 4\_2 (right)

The resulting  $U_g$  profiles for the Sugrue model, adjusted Sugrue model, and  $Wo_{new}$  model are given in Figures B-6 - B-9.

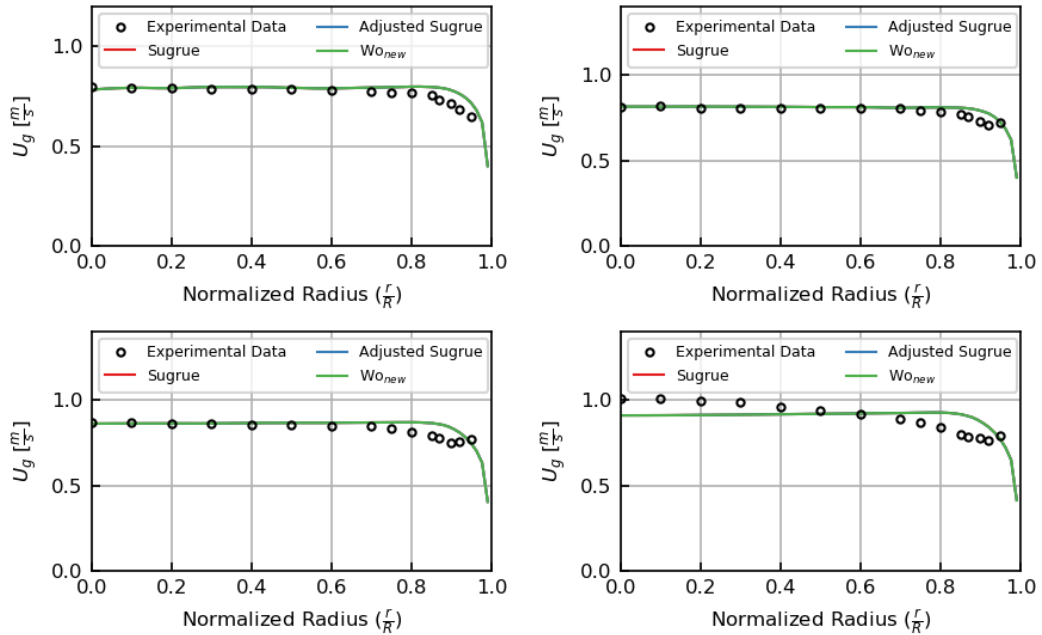


**Figure B-6:** Comparison of  $U_g$  profiles from Sugrue, the adjusted Sugrue, and  $Wo_{new}$  on Hibiki 1\_1 (top left), 1\_2 (top right), 1\_3 (bottom left), and 1\_4 (bottom right)

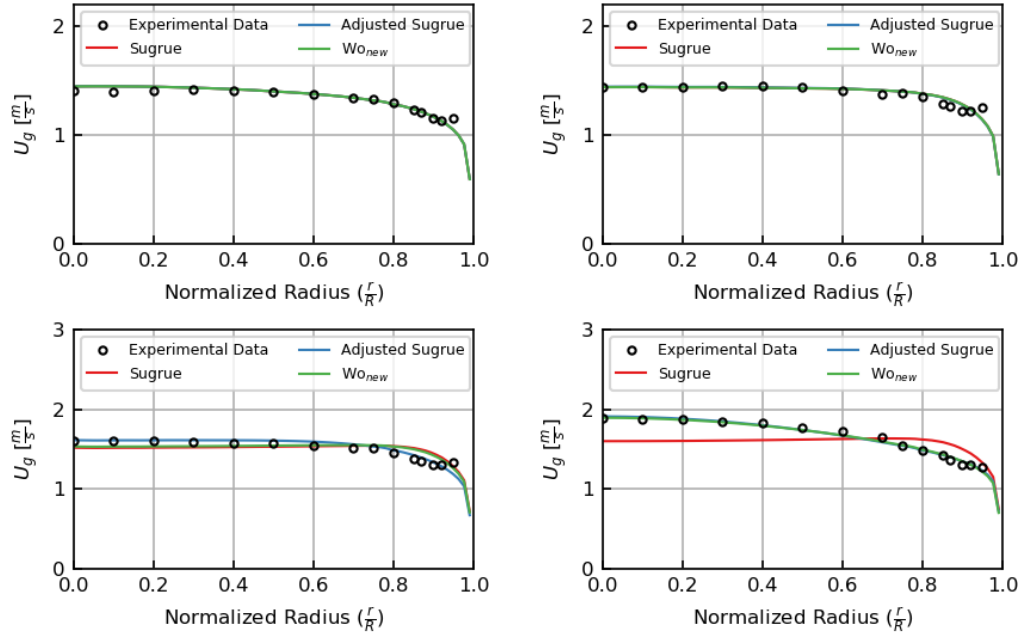


**Figure B-7:** Comparison of  $U_g$  profiles from Sugrue, the adjusted Sugrue, and  $W_{O_{new}}$  on Hibiki 2\_1 (top left), 2\_2 (top right), 2\_3 (bottom left), and 2\_4 (bottom right)

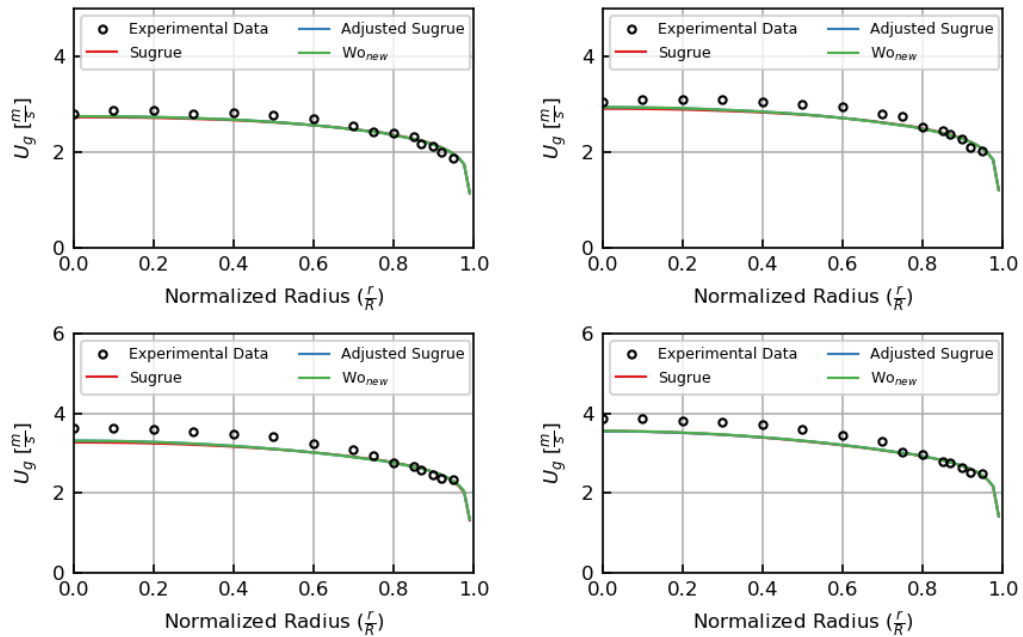


**Figure B-8:** Comparison of  $U_g$  profiles from Sugrue, the adjusted Sugrue, and  $W_{O_{new}}$  on Hibiki 3\_1 (top left), 3\_2 (top right), 3\_3 (bottom left), and 3\_4 (bottom right)

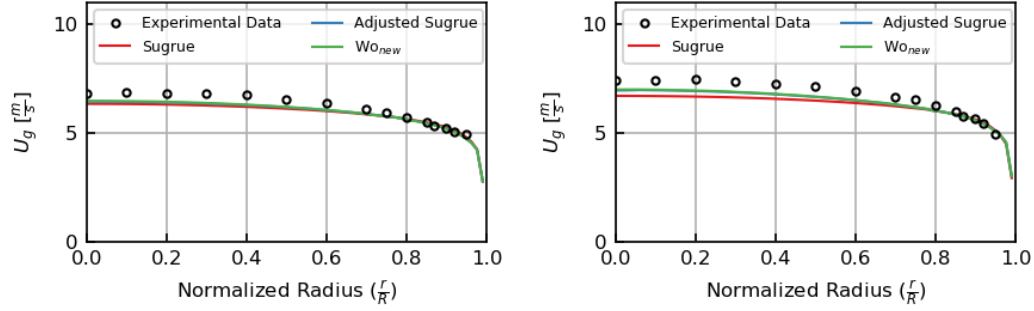


**Figure B-9:** Comparison of  $U_g$  profiles from Sugrue, the adjusted Sugrue, and  $Wo_{new}$  on Hibiki 4\_1 (left) and 4\_2 (right)

Figures B-10 and B-11 respectively are the spread error plots for  $U_l$  and  $U_g$ . In these plots, a point on the  $y = x$  line means two values are exactly equal, while the dotted lines represent a margin of  $\pm 10\%$ . Additionally the root mean squared error (RMSE) for each model across entire Hibiki experiment is compared in the legend. RMSE is calculated as

$$\text{RMSE} = \sqrt{\frac{\sum_{i=0}^n (f_{\text{experiment},i} - g_{\text{simulation},i})^2}{n}}. \quad (\text{B.1})$$

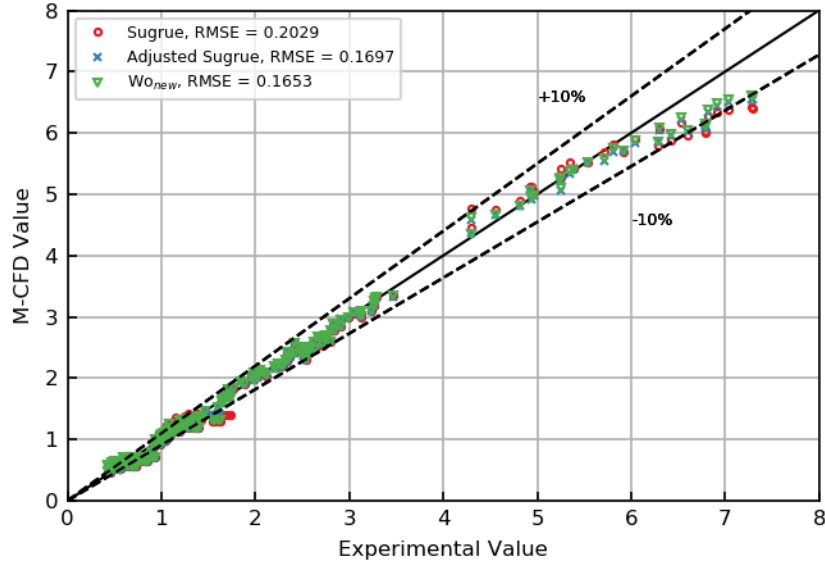


**Figure B-10:** Spread error on  $U_l$  profiles from Sugrue, the adjusted Sugrue, and  $Wo_{new}$  on Hibiki experiment

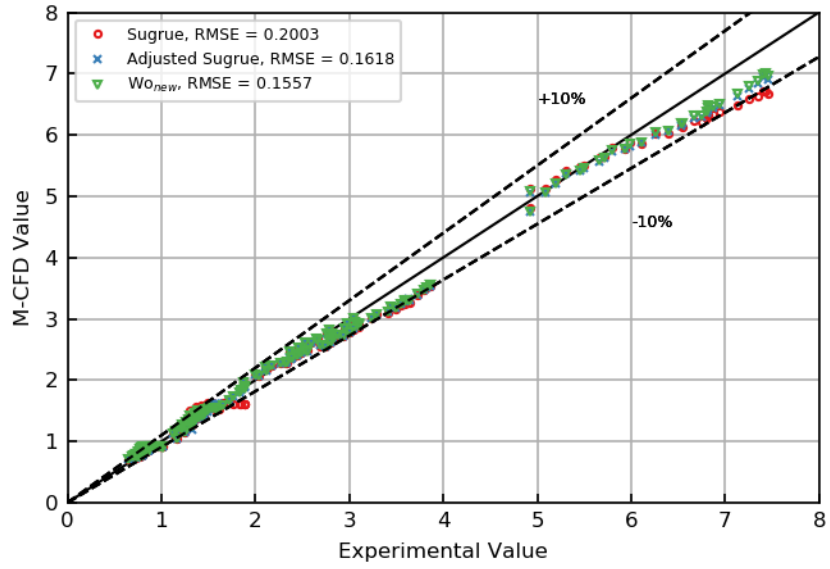


**Figure B-11:** Spread error on  $U_g$  profiles from Sugrue, the adjusted Sugrue, and  $Wo_{new}$  on Hibiki experiment





# Appendix C

## TOPFLOW Experiment

The TOPFLOW test facility at HZDR has provided an invaluable amount of CFD grade multiphase flow measurements. Among these, is a set of upward bubbly pipe flow experiments that were performed with a constant injection pressure of 0.25 MPa and a temperature of 30 °C, that measured time averaged  $\alpha_g$ ,  $U_g$ , and sauter mean bubble diameter ( $d_{32}$ ) measurements [7]. The database includes both wall and core peaked gas volume fraction distributions from air that was injected at the pipe wall, making it ideal for testing the performance of the lift momentum closure model.

### C.1 Experimental Description

The TOPFLOW experimental test section of interest was a 0.1953 m inner diameter pipe that was 8 m in length. At the top of the pipe, radial measurements of  $\alpha_g$ ,  $U_g$ , and  $d_{32}$  were recorded using a wire mesh sensor at the top of the pipe. In order to measure the development of two phase flow, air was injected at increasing flow-wise distances away from the sensor, while adjusting the system pressure to keep the injection pressure constant. The experimental test section included six air injection modules which consisted of three air injection chambers for a total of eighteen injection points denoted A-R. For each injection module, two of the three air injectors consisted of 72 equally spaced, 1 mm orifices; only the data from these air injectors was analyzed since they will produce consistent bubble sizes with each other while providing the

most data planes. Figure C-1 shows a schematic of the TOPFLOW experiment and air injectors. Meanwhile Table C.1 details the distance from the sensor for each air injection location at which the experimental and simulation data are compared.

**Table C.1:** TOPFLOW air injector distance from sensor [7]

	Injector Location					
	C	F	I	L	O	R
Distance from sensor [m]	0.335	0.608	1.552	2.595	4.531	7.802

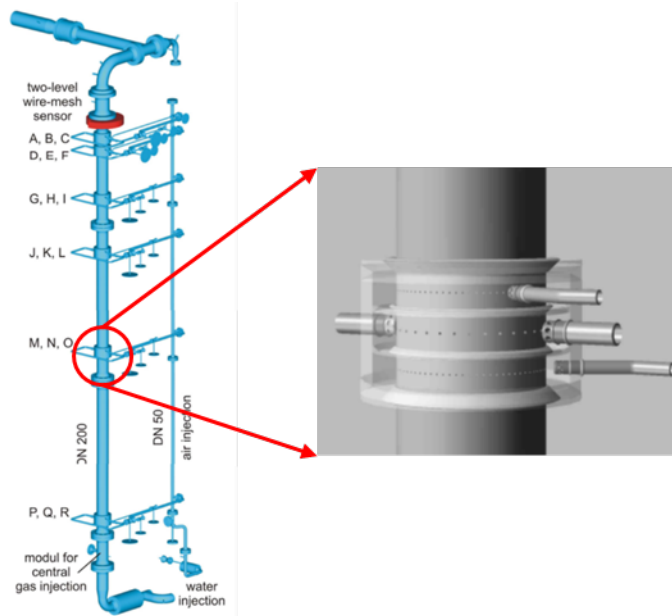


**Figure C-1:** TOPFLOW test section and air injectors of study [7]

From the experimental matrix of 48 experiments with varying liquid and gas superficial velocities, the results from eight cases are presented in this work. Each of the eight selected cases are within the bubbly flow regime and from each case the data at each of the six axial planes in Table C.1 was analyzed for this work. The superficial gas and liquid velocities for the eight analyzed cases are summarized in Table C.2.

**Table C.2:** Summary of TOPFLOW conditions [7]

Experimental Set	Superficial liquid velocity [ $\frac{m}{s}$ ]	Superficial gas velocity [ $\frac{m}{s}$ ]
006	0.405	0.0025
028	0.405	0.0062
050	0.405	0.0151
072	0.405	0.0368
008	1.017	0.0025
030	1.017	0.0062
052	1.017	0.0151
074	1.017	0.0368

## C.2 Simulation Set Up

The TOPFLOW experiments were simulated as a quarter pipe using STAR-CCM+ v13.06.011 on developing bubbly flow on the selected eight experiments. The quarter pipe was modeled with separate air and water inlets keeping the pressure constantly set to 0.25 MPa at the air inlet. A quarter of the pipe was used to take advantage of symmetry to reduce the number of cells required for improved computational efficiency. At the water inlet, a fully developed turbulent flow profile was specified.

The computational geometry for the two-phase simulation was a quarter pipe with a diameter of 0.1953 m and a length of 8.2 m. The pipe wall has a no-slip velocity condition applied while for the remaining two walls symmetry conditions are adopted. The pipe outlet was set to a pressure outlet. The air inlet was set as a 6 mm tall slice of the pipe wall centered at  $z = 0$  m where a uniform velocity profile of air was injected at the velocity necessary to match each experiment's mass flow rate of air. The computational data planes are set at heights equal to the distances of the injection planes in Table C.1. A fully developed turbulent flow profile was injected at the water inlet, 20 cm upstream of the air inlet.

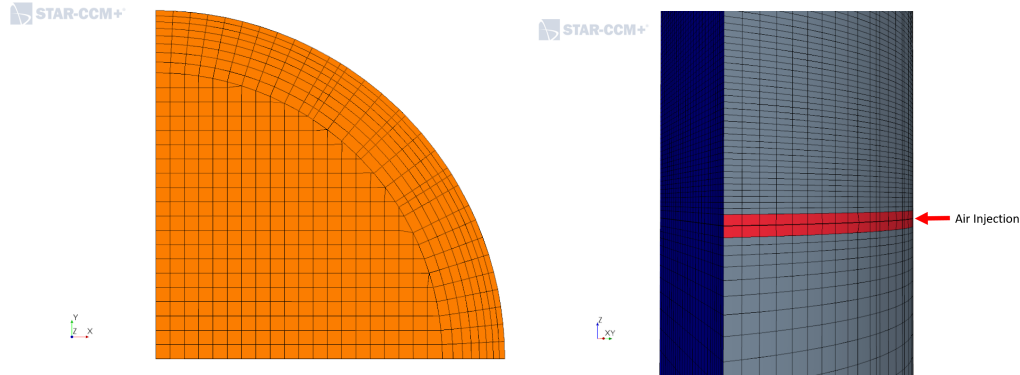


**Figure C-2:** TOPFLOW computational mesh

The mesh has a base size of 4 mm in the bulk. A total prism layer thickness of 17.45 mm was set with 8 prism layers and a stretching of 1.1. The mesh was extruded axially in both the  $+Z$  and  $-Z$  direction from the air injection utilizing a hyperbolic tangent mesh extrusion. At the outlet the mesh cells are 15 mm in the flow wise direction for an aspect ratio of 3.75. FigureC-2 shows the computational mesh and geometry. The simulations were performed using experimental bubble diameter profiles varying radially for each respective height. Where the experimental bubble diameter was zero the minimum non-zero value of bubble diameter for that height was specified. This approach allows eliminating potential inaccuracy related to interfacial area predictions, in order to best evaluate the effect of momentum closures.

The other models used were consistent with the Bubbly And Moderate void Fraction (BAMF) framework [3, 17, 23]. The models selected are:

1. Turbulence: Standard  $k-\epsilon$  scaled by liquid volume fraction
2. Drag: Tomiyama moderately contaminated drag [32] with no swarm correction
3. Turbulent dispersion: Burns [18]
4. Interfacial area: Experimental sauter mean diameter values prescribed at each height
5. Near wall models:

- Turbulence: High  $y^+$  model
- Lift: Podowski near wall correction [33]
- Wall lubrication: Lubchenko [17]

### C.3 Velocity Results

The resulting  $U_l$  profiles for the Sugrue model, adjusted Sugrue model, and  $Wo_{new}$  model are given in Figures C-3 - C-6.

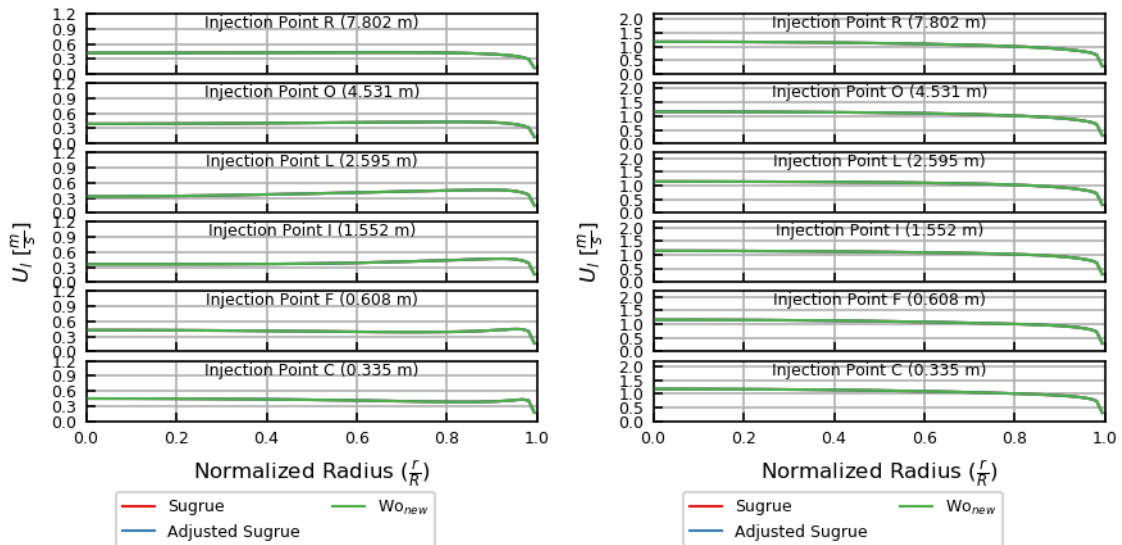


**Figure C-3:** Comparison of  $U_l$  profiles from Sugrue, the adjusted Sugrue, and  $Wo_{new}$  on TOPFLOW 006 (left) and 008 (right)

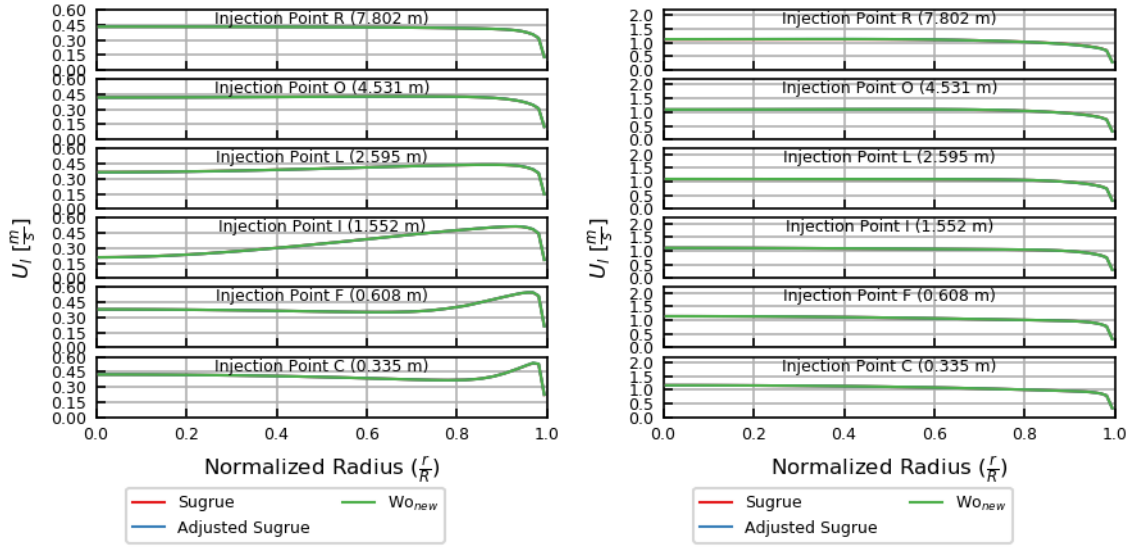


**Figure C-4:** Comparison of  $U_l$  profiles from Sugrue, the adjusted Sugrue, and  $Wo_{new}$  on TOPFLOW 028 (left) and 030 (right)

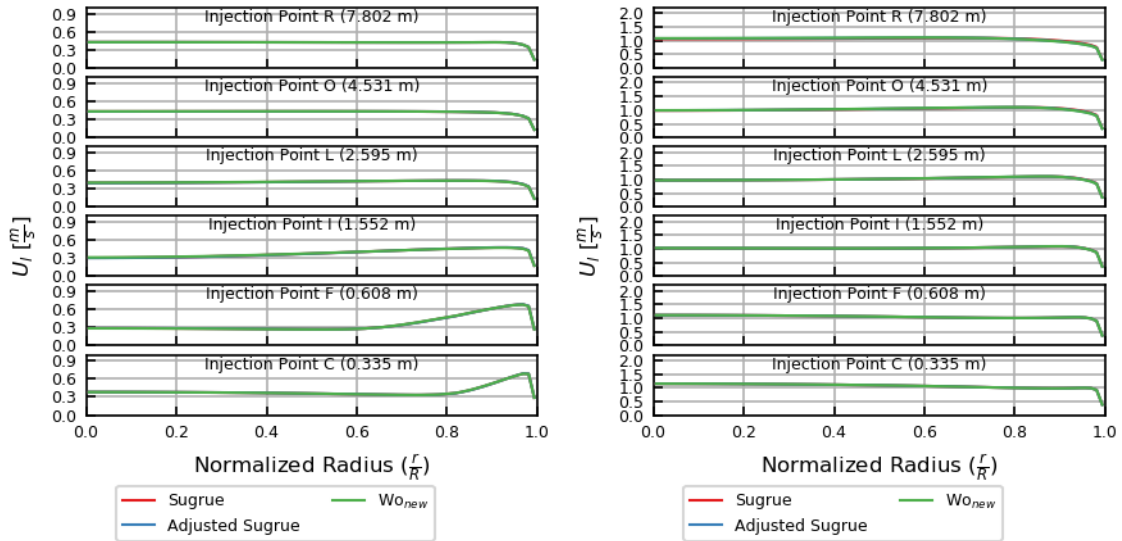


**Figure C-5:** Comparison of  $U_l$  profiles from Sugrue, the adjusted Sugrue, and  $Wo_{new}$  on TOPFLOW 050 (left) and 052 (right)

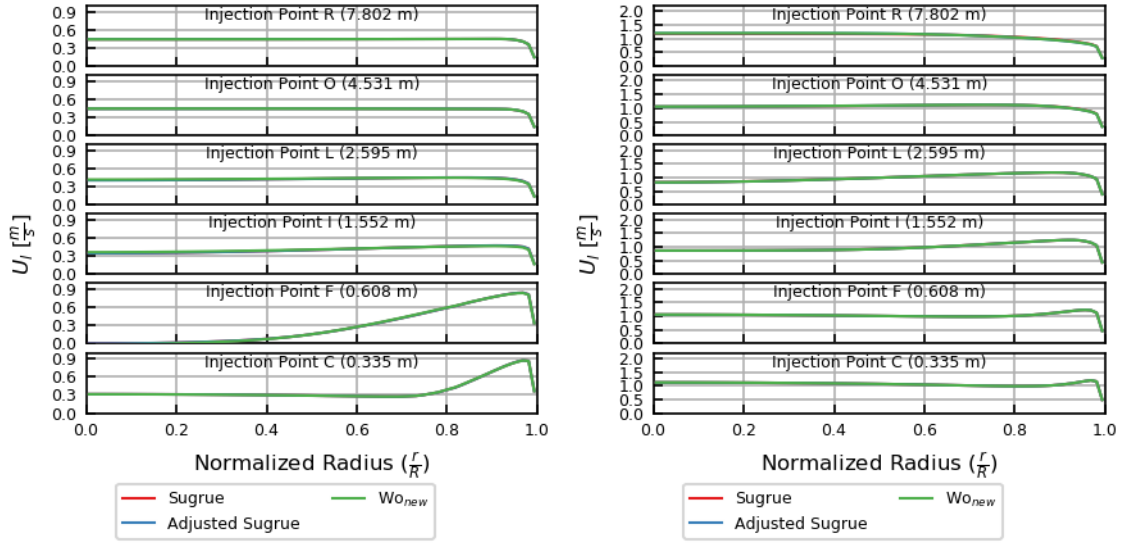


**Figure C-6:** Comparison of  $U_l$  profiles from Sugrue, the adjusted Sugrue, and  $Wo_{new}$  on TOPFLOW 072 (left) and 074 (right)

The resulting  $U_g$  profiles for the Sugrue model, adjusted Sugrue model, and  $Wo_{new}$  model are given in Figures C-7 - C-10.

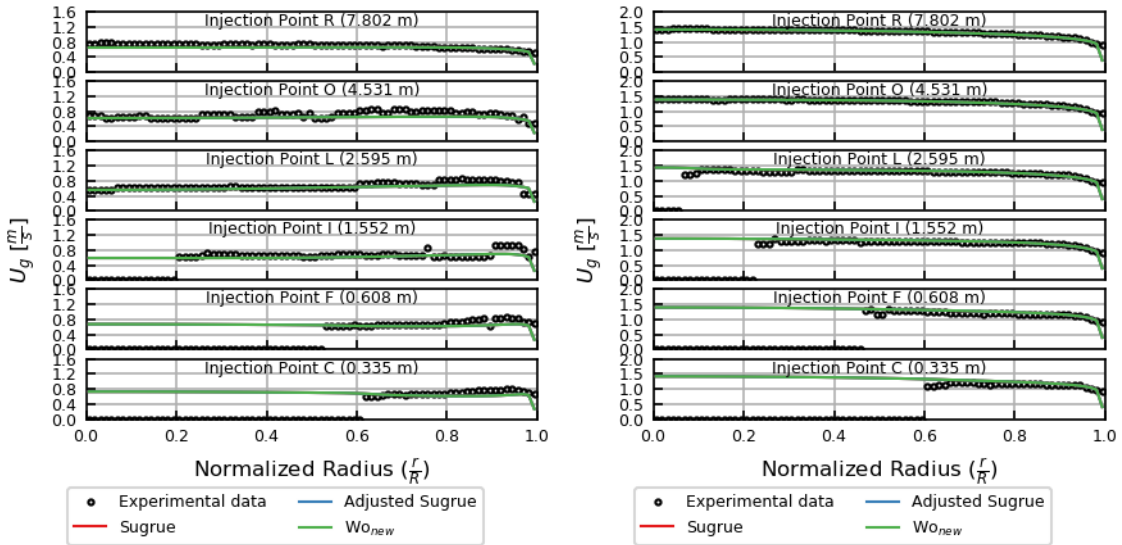


**Figure C-7:** Comparison of  $U_g$  profiles from Sugrue, the adjusted Sugrue, and  $Wo_{new}$  on TOPFLOW 006 (left) and 008 (right)

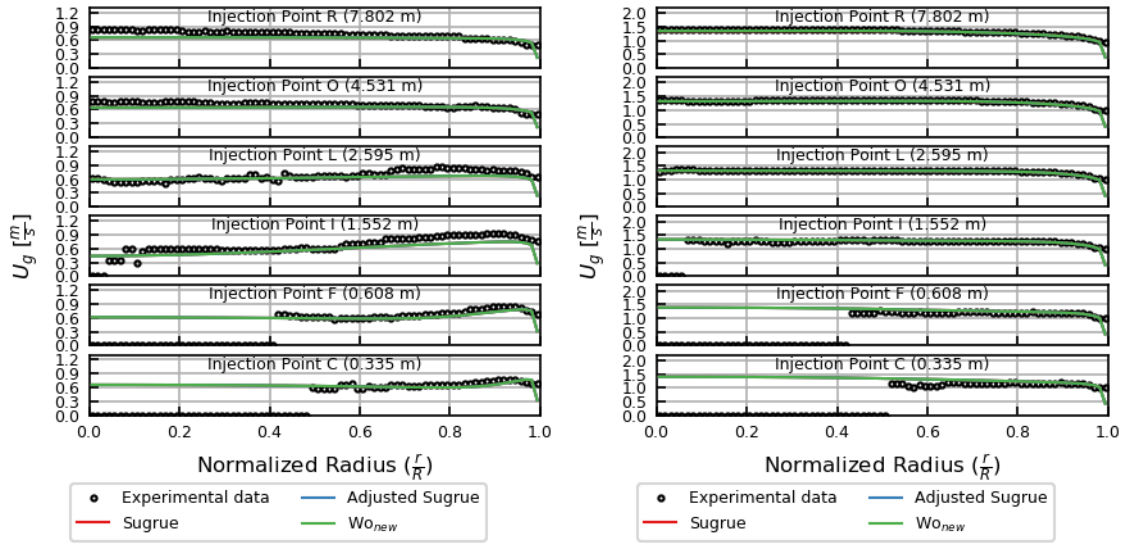


**Figure C-8:** Comparison of  $U_g$  profiles from Sugrue, the adjusted Sugrue, and  $Wo_{new}$  on TOPFLOW 028 (left) and 030 (right)

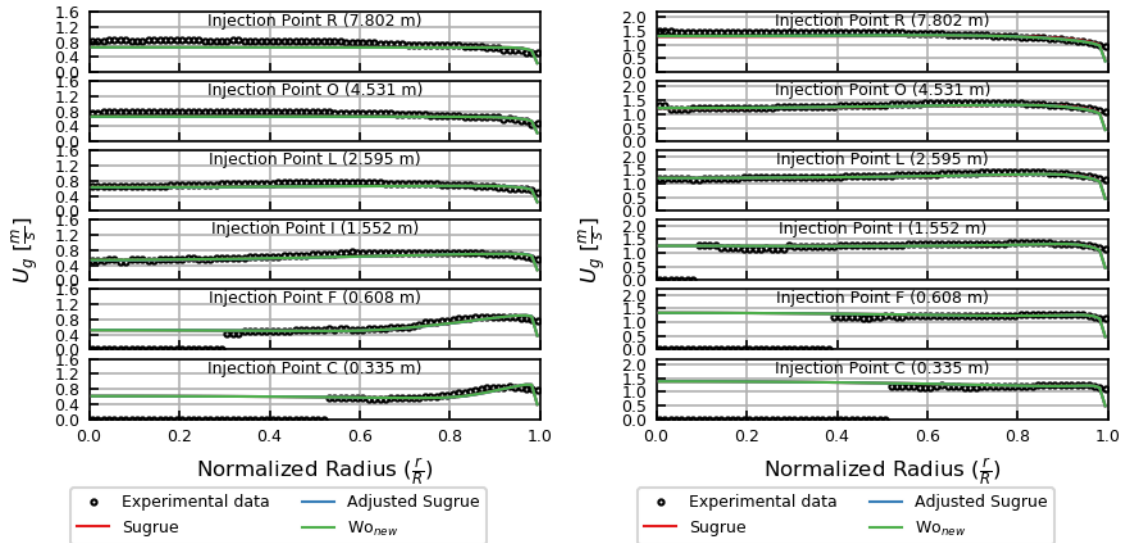


**Figure C-9:** Comparison of  $U_g$  profiles from Sugrue, the adjusted Sugrue, and  $Wo_{new}$  on TOPFLOW 050 (left) and 052



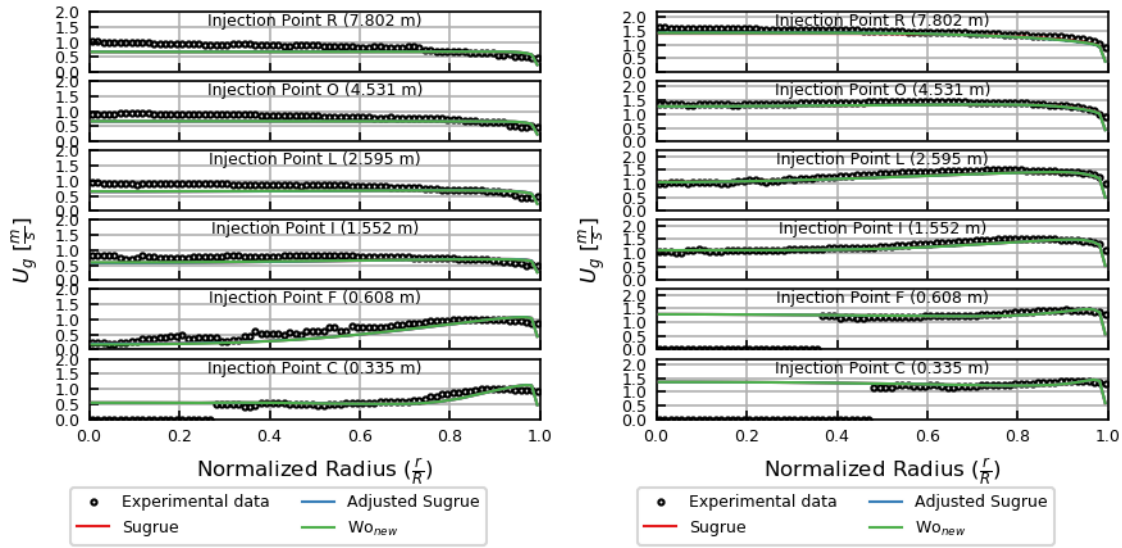


**Figure C-10:** Comparison of  $U_g$  profiles from Sugrue, the adjusted Sugrue, and  $Wo_{new}$  on TOPFLOW 072 (left) and 074 (right)

Figure C-11 is the spread error plots for  $U_g$ . In this plot, a point on the  $y = x$  line means two values are exactly equal, while the dotted lines represent a margin of  $\pm 10\%$ . Additionally the root mean squared error (RMSE, equation B.1) for each model across entire TOPFLOW experiment is compared in the legend.

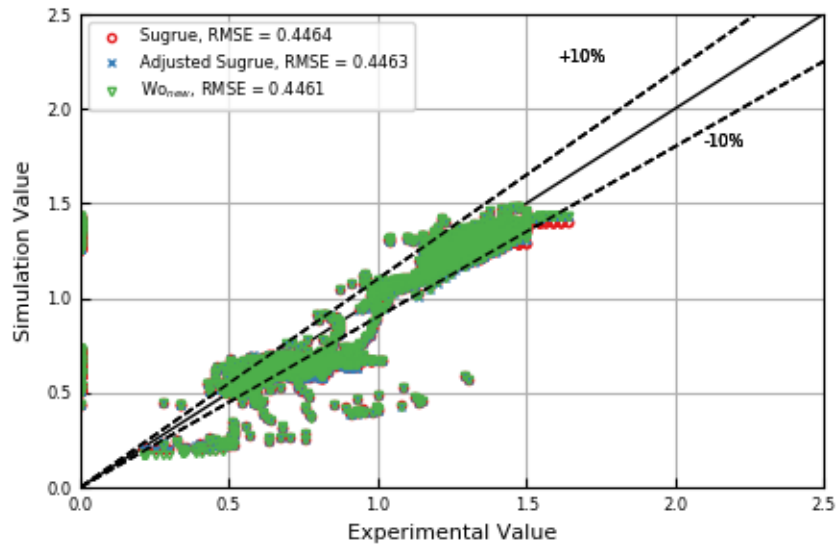


**Figure C-11:** Spread error on  $U_g$  profiles from Sugrue, the adjusted Sugrue, and  $Wo_{new}$  on TOPFLOW experiment



# Appendix D

## Fully Developed Bubbly Flow

Leveraging the findings from Lubchenko [17] and the current understanding of lift [3], in a fully developed, two-phase flow  $\alpha_g$  should either peak in the pipe center if  $C_L$  is predominantly negative, peak one bubble radius from the wall if  $C_L$  is predominantly positive (as it represents the center of the layer of bubble accumulation near the wall), or be flat if the effects of turbulent dispersion are greater than those of lift. From studying the TOPFLOW data, which recovers the flow profile of developing, two-phase flow, this understanding is supported. On the left side of Figure D-1, it can be observed that the  $\alpha_g$  peak for TOPFLOW 074 does move away from the wall, but ends in the pipe center at 8 m. At 0.6, 1.5, 2.6, and 4.5 m, the  $\alpha_g$  move from the wall to outside of one bubble radius but clearly is migrating to the pipe center. Therefore the assertion that a more positive  $C_L$  needs to be predicted from the analysis of the TOPFLOW experiment at the 4.5 m data plane [4] is not made based off a fully developed profile.

Hibiki experiments 3\_1 and 3\_2 show a off-wall  $\alpha_g$  peak just like the developing TOPFLOW experiment 074 data.  $\alpha_g$  for Hibiki 3\_2 is shown on the right side of Figure D-1 for a side by side comparison of the two profiles. It is possible that as the bubbles migrated to the wall in Hibiki 3\_2, coalesced, then began migrating back to the pipe center; meaning that this flow profile is not fully developed. Therefore missing these two cases in the adjusted Sugrue model in Chapter 4 is not a large

concern.

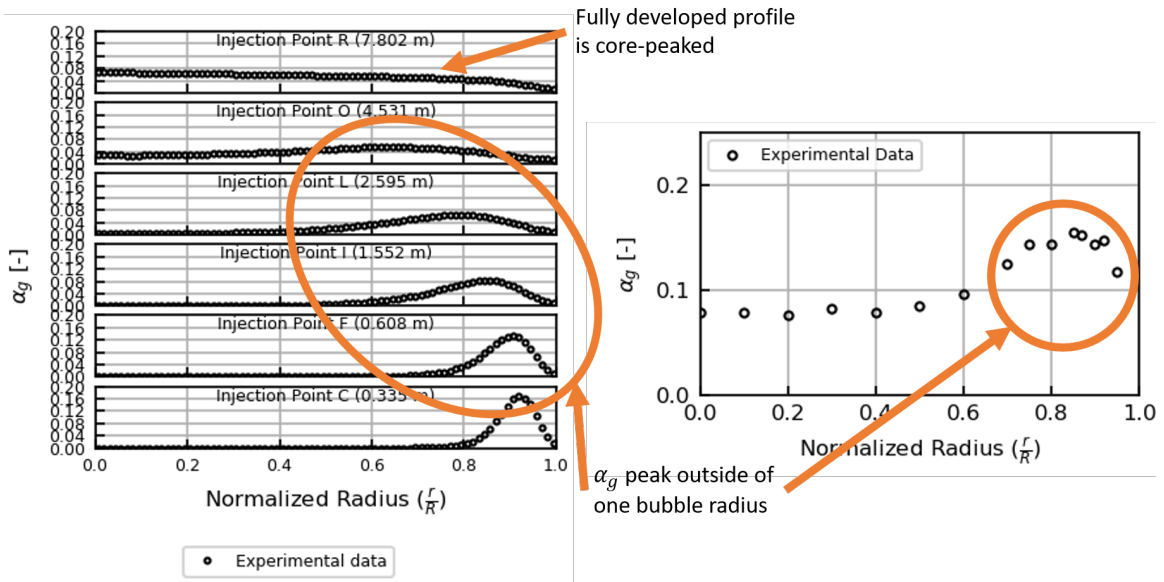


**Figure D-1:** Comparison of the developing  $\alpha_g$  profile from TOPFLOW 074 (left) to Hibiki 3\_2 (right), showing that Hibiki experiments 3\_1 and 3\_2 may not be fully developed flow

# Appendix E

## Changes from the Sugrue Model

Implementing the Sugrue model as described in Sugrue's thesis [3], the results on the Hibiki experiment do not match those shown in the thesis. Figures E-1 - E-3 compare the originally reported results from the Sugrue model to those obtained in this work. From further study of the Sugrue model's implementation in Appendix A of the thesis [3] the implementation used  $Eo_d$  instead of  $Eo$  in  $Wo$ . There are only slight changes in  $\alpha_g$  predictions when from switching to  $Eo_d$  from  $Eo$ , and the results from Sugrue's thesis still could not be replicated, even mimicking the original implementation. For the adjusted Sugrue and  $Wo_{new}$  models moving forward,  $Eo$  is used.

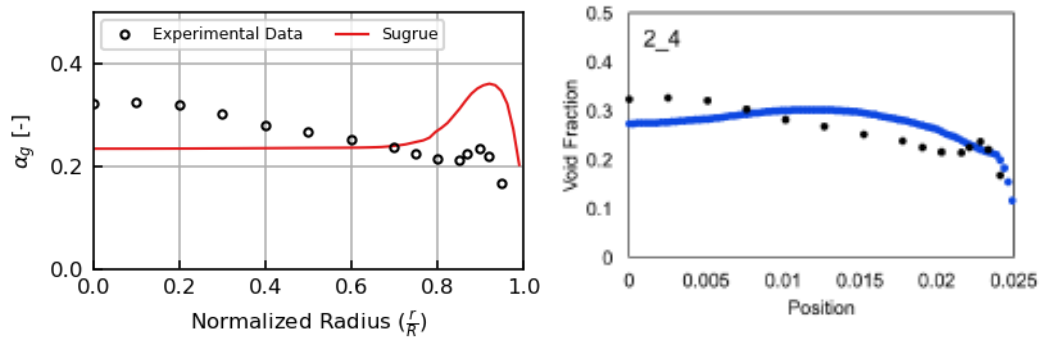


**Figure E-1:** Sugrue difference and difficulty on Hibiki 2\_4

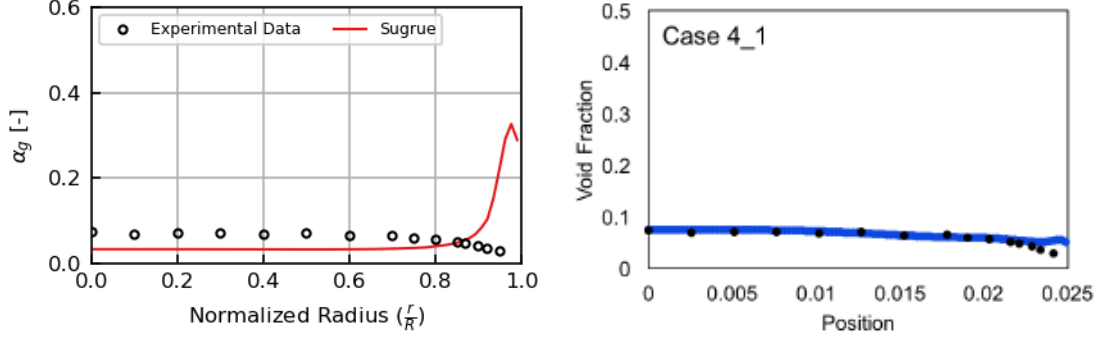


**Figure E-2:** Sugrue difference and difficulty on Hibiki 4\_1

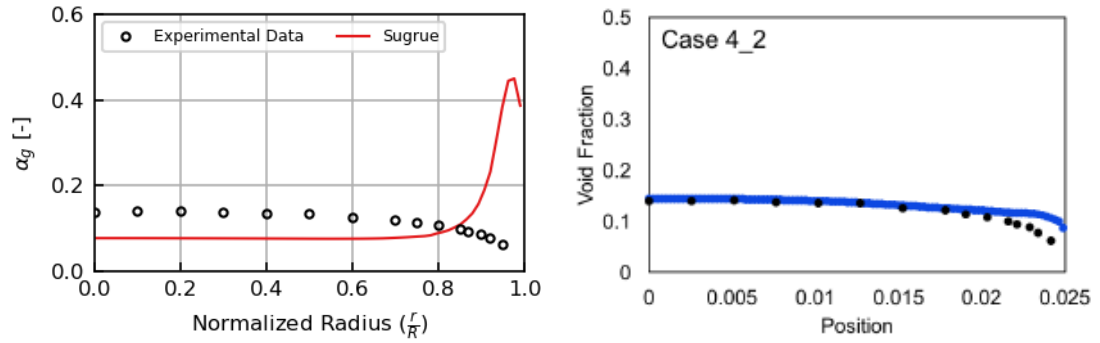


**Figure E-3:** Sugrue difference and difficulty on Hibiki 4\_2

Additionally, the swarm correction,  $f(\alpha_g)$ , is also corrected for a typo in the original implementation. The function is changed from

$$f(\alpha_g) = \min[1, 1.0155 - 1.0154 \exp(8.0506\alpha_g)] \quad (\text{E.1})$$

as implemented in Sugrue's thesis Appendix A [3] to

$$f(\alpha_g) = \max[0, 1.0154 - 1.0154 \exp(8.0506\alpha_g)]. \quad (\text{E.2})$$

This recovers the intended model behavior without allowing the swarm correction to be negative. It also ensures that the value of  $f(\alpha_g)$  goes from 1 to 0 between  $0.2 < \alpha_g < 0.52$  as originally intended.